Critical magnetic fluctuations in the layered ruthenates Ca_2RuO_4 and $Ca_3Ru_2O_7$

H. Trepka,[1,2] T. Keller,[1,2] M. Krautloher,[1] J. Xu,[3] K. Habicht,[3,4] M. Böhm,[5] B. Keimer,[1,*] and M. Hepting[1,2,†]

[1]*Max-Planck-Institute for Solid State Research, Heisenbergstraße 1, 70569 Stuttgart, Germany*

[2]*Max Planck Society Outstation at the Heinz Maier-Leibnitz Zentrum (MLZ), Lichtenbergstraße 1, 85748 Garching, Germany*

[3]*Helmholtz-Zentrum Berlin für Materialien und Energie, Hahn-Meitner Platz 1, D-14109 Berlin, Germany*

[4]*Institut für Physik und Astronomie, Universität Potsdam, Karl-Liebknecht-Straße 24-25, 14476 Potsdam, Germany*

[5]*Institut Laue-Langevin, 71 Avenue des Martyrs, 38042 Grenoble Cedex 9, France*

(Received 22 December 2021; accepted 10 May 2022; published 3 June 2022)

Materials realizing the XY model in two dimensions are sparse. Here we use neutron triple-axis spectroscopy to investigate the critical static and dynamical magnetic fluctuations in the square-lattice antiferromagnets Ca_2RuO_4 and $Ca_3Ru_2O_7$. We probe the temperature dependence of the antiferromagnetic Bragg intensity, the Q width, the amplitude, and the energy width of the magnetic diffuse scattering in the vicinity of the Néel temperature T_N to determine the critical behavior of the magnetic order parameter M, correlation length ξ, susceptibility χ, and the characteristic energy Γ with the corresponding critical exponents β, ν, γ, and z, respectively. We find that the critical behaviors of the single-layer compound Ca_2RuO_4 follow universal scaling laws that are compatible with predictions of the two-dimensional (2D) XY model. The bilayer compound $Ca_3Ru_2O_7$ is only partly consistent with the 2D XY theory and best described by the three-dimensional (3D) Ising model, which is likely a consequence of the intrabilayer exchange interactions in combination with an orthorhombic single-ion anisotropy. Hence, our results suggest that layered ruthenates are promising solid-state platforms for research on the 2D XY model and the effects of 3D interactions and additional spin-space anisotropies on the magnetic fluctuations.

DOI: 10.1103/PhysRevResearch.4.023181

I. INTRODUCTION

Critical fluctuations of the order parameter emerge in proximity to the transition temperature T_c of second-order phase transitions. These fluctuations are characterized by a correlation length ξ and a response time τ, which diverge at T_c [1–4]. In the critical regime close to T_c, fundamental physical properties of a material, such as the magnetic susceptibility and the heat capacity, adopt critical behavior and can be described by power laws (PLs) $\propto |t|^{\lambda}$, with critical exponents λ and $t \equiv (T/T_c - 1)$ [2–6]. Furthermore, the scaling behaviors in the spatial and time domains are related via $\Gamma \propto \kappa^z \propto t^{z\nu}$ [3], with the critical exponents ν of the inverse correlation length $\kappa = \xi^{-1}$ and z of the characteristic energy $\Gamma \propto \tau^{-1}$. A hallmark of the corresponding scaling theory is the concept of universality [4,7,8], which stipulates that (for systems with short-range interactions) the critical exponents are independent of microscopic details, and depend exclusively on the dimensionality of space and the dimensionality of the order parameter. In magnetic systems, the scaling behavior of magnetic critical fluctuations thus encodes the spatial dimensionality of the system and possible magnetic anisotropies [4]. Along these lines, in particular the two-dimensional (2D) XY model has attracted significant attention, since it was employed as the model system for the unconventional vortex-unbinding transition proposed by Berezinskii, Kosterlitz, and Thouless (BKT) [9–11]. The fingerprints of BKT transitions were observed in superfluid ^{4}He films [12,13] and proximity-coupled Josephson-junction arrays [14,15]. Yet, solid-state materials that realize the 2D XY model are sparse [16–20].

A key experimental technique for the investigation of critical magnetic scattering is neutron triple-axis spectroscopy (TAS), which exploits the proportionality between the magnetic neutron-scattering cross section and the dynamic scattering function $S(\boldsymbol{q}, \omega)$, containing κ and Γ [21–23]. More specifically, Γ can be derived from TAS energy scans of the critical magnetic scattering, while κ corresponds to the energy-integrated Q width in momentum space. Along these lines, pioneering studies investigated the critical magnetic fluctuations in classical magnetic systems, such as the three-dimensional (3D) ferromagnet (FM) EuO [24–26] and the 3D antiferromagnet (AFM) $RbMnF_3$ [27,28]. Furthermore, TAS studies were carried out on systems with quasi-2D magnetic correlations, including the isotropic square-lattice AFMs Rb_2MnF_4 [29], $Sr_2CuO_2Cl_2$, and $Sr_2Cu_3O_4Cl_2$ [30], as well as the AFM parent compounds of the cuprate superconductors [31], which exhibit 2D Heisenberg (2D-H) scaling properties above their Néel temperatures. More recently,

*B.Keimer@fkf.mpg.de
†Hepting@fkf.mpg.de

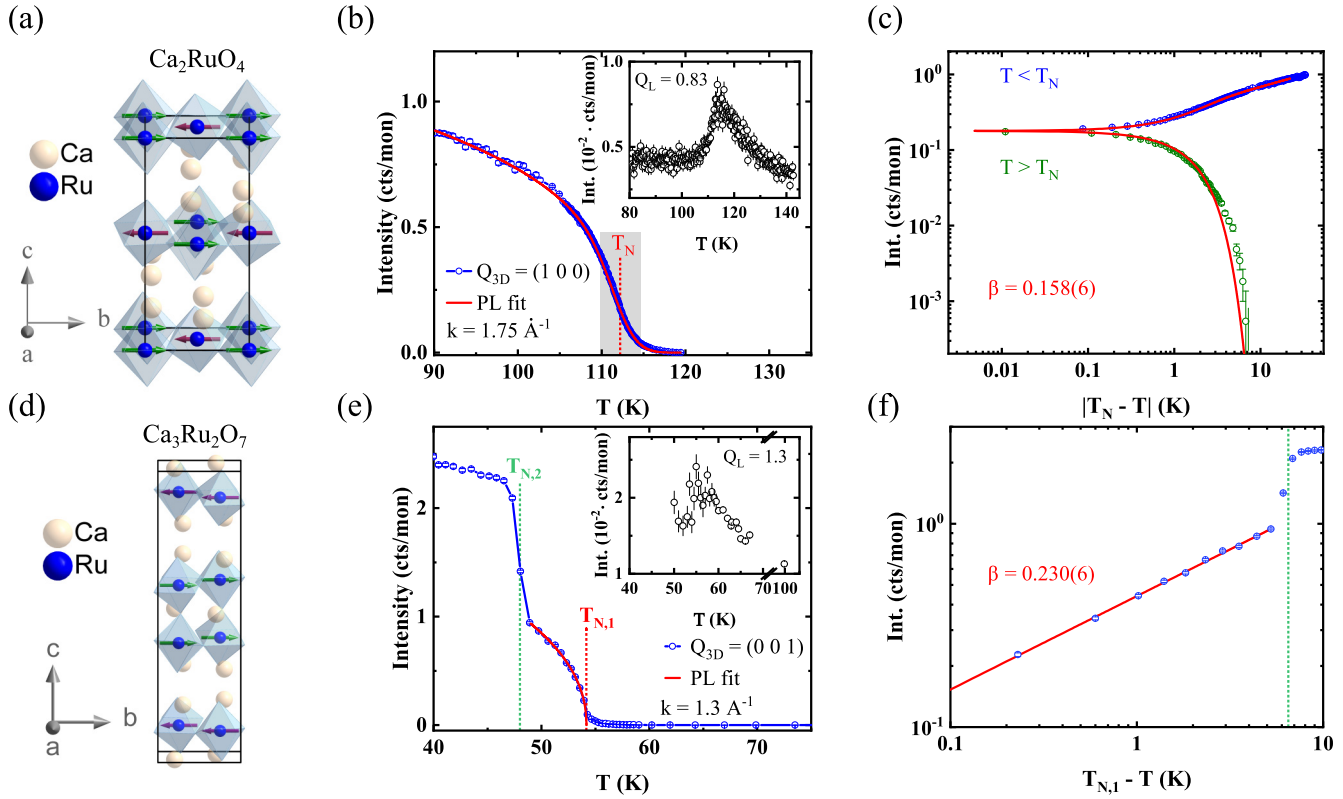

FIG. 1. Crystal structure, critical scattering, and magnetic order parameter in Ca_2RuO_4 (a–c) and $Ca_3Ru_2O_7$ (d–f). (a) Schematic of the crystallographic unit cell of single-layer Ca_2RuO_4 (black lines). Oxygen ions are omitted for clarity. Green and purple spins indicate the G-type AFM order. (b) Intensity of the magnetic (1 0 0) peak measured as a function of temperature. The red solid line is a PL fit $I \propto M^2 \propto |t|^{2\beta}$, with $\beta = 0.158(6)$ and $T_N = 112.20(1)$ K, convoluted with a Gaussian distribution of Néel temperatures T_N with a FWHM of 4.84(1) K (gray shaded area). The inset shows the intensity measured at $Q = (1\,0\,0.83)$. The increase of intensity in the vicinity of T_N indicates the presence of critical scattering from critical magnetic fluctuations. (c) Same data as in panel (b), but on a double-logarithmic scale. Note that the data and fits are nonlinear due to the distribution of T_N. (d) Schematic of the unit cell of bilayer $Ca_3Ru_2O_7$ (black lines) with the A-type AFM order indicated. (e) Intensity of the magnetic (0 0 1) peak. The green and red dashed lines indicate the two AFM transitions. Below $T_{N,2} = 48$ K, the magnetic moments reorient from $m \parallel a$ to $m \parallel b$. The red solid line is a PL fit, which yields $T_{N,1} = 54.16(2)$ K and $\beta = 0.230(6)$. The inset shows the intensity measured at $Q = (0\,0\,1.3)$, with the increase of intensity in the vicinity of $T_N \approx 54$ K indicating the presence of critical scattering. (f) Same data for $T < T_{N,1}$ as in panel (e), but on a double-logarithmic scale.

critical magnetic fluctuations were investigated in 5*d*-electron transition-metal oxides (TMOs) using x-ray scattering. In single-layer Sr_2IrO_4, which exhibits a Mott-insulating AFM ground state with a $J_{\text{eff}} = 1/2$ effective total angular momentum due to strong spin-orbit coupling (SOC) [32,33], 2D-H scaling with a small easy-plane anisotropy was reported [34,35]. On the other hand, in bilayer $Sr_3Ir_2O_7$ the scaling behavior close to the transition is consistent with the 3D Ising (3D-I) universality class, but significant deviations were found and attributed to disorder [36].

In 4*d*-electron TMOs, such as single- and bilayer ruthenates, critical fluctuations have remained unexplored to date. Notably, ruthenates show a plethora of electronic ground states [37–41] such as unconventional superconductivity in Sr_2RuO_4 [42] and excitonic AFM order in the Mott insulator Ca_2RuO_4 [43,44], arising from a delicate competition between the energy scales of SOC, crystal-field splitting, Hund's coupling, and inter-site exchange interactions. In the latter compound, spins are arranged in an AFM fashion within square-lattice RuO_2 planes and stacked along the *c* axis in a G-type pattern [Fig. 1(a)] with a Néel temperature $T_N \approx 110$ K [45–47]. The excitonic character is believed to result from excitonic transitions between nonmagnetic singlet ($J_{\text{eff}} = 0$) and magnetic triplet states ($J_{\text{eff}} = 1$) [43,44]. The nature of the excitonic magnetism was recently corroborated by resonant inelastic x-ray scattering (RIXS) [48], Raman scattering [49], as well as inelastic neutron scattering (INS), detecting a soft amplitude mode ("Higgs mode") in the spin-wave spectrum [50].

The unquenched orbital angular momentum of the Ru magnetic moments in Ca_2RuO_4 further results in a highly unusual spectrum of transverse magnons in the AFM state [50]. The low-energy magnetic Hamiltonian derived from an analysis of this spectrum is dominated by an *XY*-type single-ion anisotropy, which is larger than the nearest-neighbor exchange interaction, and an Ising-type single-ion anisotropy resulting from an orthorhombic distortion of the crystal structure. At the same time, the INS experiments did not reveal any dispersion of the magnons perpendicular to the RuO_2 layers, which implies that the interlayer interactions are much weaker than the interactions within the layers. The evidence for an approximate 2D *XY* symmetry of the magnetic Hamiltonian derived

from the analysis of the magnon dispersions has motivated the present paper.

In contrast to the Mott insulator Ca_2RuO_4, the bilayer compound $Ca_3Ru_2O_7$ is metallic in the paramagnetic state and maintains considerable electrical conductivity below the Néel temperature $T_{N,1} \approx 56$ K [51]. The magnetic structure is A-type AFM (i.e., FM bilayers with alternating orientation along the c axis) [Fig. 1(d)] [51,52]. A second magnetic transition associated with a reorientation of the spins from the a to the b axis in the RuO_2 planes [53] and a greater reduction of the electrical conductivity occurs at $T_{N,2} \approx 48$ K [51]. As the crystal structure of $Ca_3Ru_2O_7$ is composed of two closely spaced RuO_2 layers within a unit cell [Fig. 1(d)], substantial interlayer interactions within a bilayer unit are expected and were indeed identified in INS studies of the magnon dispersions [54,55]. As exchange interactions between bilayer units are weak, the dimensionality of the exchange-bond network is intermediate between 2D and 3D cases. The INS data also revealed an anisotropy gap, but were insufficient for a determination of the nature of the dominant anisotropy (Ising versus XY).

In this paper, we use TAS to examine the critical scattering in single-layer Ca_2RuO_4 and bilayer $Ca_3Ru_2O_7$ in the vicinity of and above T_N. We extract the critical static and dynamical exponents to determine the spin dimensionalities and anisotropies, which we compare to the model Hamiltonians employed in previous INS and RIXS studies below T_N. For Ca_2RuO_4, we derive the critical exponent β of the order parameter from the temperature dependence of the AFM (1 0 0) Bragg intensity. The static critical exponents ν and γ are extracted from the Q width and amplitude, respectively, of the magnetic diffuse scattering around (1 0 0.83) above T_N. We find that the temperature dependence of the order parameter, Q width, and amplitude are well captured by a 2D XY model, as expected based on the spin Hamiltonian extracted from the magnon dispersions [50]. The dynamic critical exponent z is derived from the broadening in energy of the diffuse scattering at (1 0 0) for $T > T_N$ and is also in reasonable agreement with the 2D XY model. For $Ca_3Ru_2O_7$, we derive β from the temperature dependence of the AFM (0 0 1) Bragg intensity below T_N, while ν, γ, and z are extracted from the Q width, amplitude, and energy width, respectively, of the diffuse scattering around (0 0 1) above T_N. From a combined consideration of all extracted exponents, we conclude that the critical behavior of $Ca_3Ru_2O_7$ is only partly consistent with the 2D XY model, and is best described by the 3D-I model. We discuss these observations in the context of prior experiments on single-layer and bilayer iridates [34–36].

II. METHODS

High-quality single crystals of Ca_2RuO_4 and $Ca_3Ru_2O_7$ were grown by the optical floating-zone method [47], as described in Ref. [50]. Ca_2RuO_4 exhibits the orthorhombic space group $Pbca$ at 11 K and the lattice parameters $a = 5.39$ Å, $b = 5.63$ Å, and $c = 11.75$ Å [45]. $Ca_3Ru_2O_7$ crystallizes in the orthorhombic space group $Bb2_1m$ at 50 K with the lattice parameters $a = 5.36$ Å, $b = 5.53$ Å, and $c = 19.54$ Å [52]. Single crystals that included orthorhombic (a, b) twins were coaligned on Si plates with thicknesses of 0.5 mm and arranged in Al-sample holders. In the case of Ca_2RuO_4, approximately 100 single crystals were coaligned, yielding a total mass of 1.5 g. In the case of $Ca_3Ru_2O_7$, approximately 30 single crystals were used with total mass of 0.8 g. The mosaicity of both sample arrays was 2°–3°. Due to the (a, b) twinning, the scattering planes were (H 0 L)/(0 K L). All values of Q are given in reciprocal-lattice units.

The two-axis mode experiments on Ca_2RuO_4 were carried out at the thermal neutron spectrometer TRISP [56,57] at the FRM II neutron source at the Heinz Maier-Leibnitz Zentrum, Garching. The instrument was operated with clockwise scattering sense at the monochromator and sample ($SM = -1$, $SS = -1$) at $k_i = 1.75$ Å^{-1}. Additionally, first neutron spin-echo (NSE) measurements were conducted at $Q = (1\,0\,0)$ with $k_i = 2.66$ Å^{-1} (TAS energy resolution/vanadium width ≈1 meV) and the instrumental configuration $SM = -1$, $SS = -1$, and $SA = -1$. The dynamic properties were measured at the cold neutron TAS FLEXX [58] at the BER II neutron source at the Helmholtz-Zentrum Berlin, Berlin. An instrumental configuration $SM = -1$, $SS = 1$, $SA = -1$, an open collimation, and a neutron wave vector $k_f = 1.3$ Å^{-1} were used. The energy resolution was ≈0.15 meV. A Be filter in addition to a velocity selector in the primary spectrometer was used to suppress higher monochromator orders. A small offset in the thermometry between TRISP and FLEXX was corrected by comparing the (1 0 0) peak intensities.

The experiments on $Ca_3Ru_2O_7$ [59] were carried out at ThALES [60], which is a cold neutron TAS at the Institut Laue-Langevin (ILL), Grenoble. The instrument was operated (i) in two-axis mode with $SM = 1$, $SS = -1$ and $k_i = 1.3$ Å^{-1} and (ii) in three-axis mode with $SM = 1$, $SS = -1$, $SA = 1$ and $k_f = 1.3$ Å^{-1} with double focusing monochromator and analyzer (energy resolution ≈0.08 meV). A Be filter was used to suppress higher monochromator orders.

The cross section of magnetic neutron scattering [21,61] is proportional to the dynamic scattering function $S(\boldsymbol{q}, \omega)$, with $\boldsymbol{Q} = \boldsymbol{G}_m + \boldsymbol{q} = \boldsymbol{k}_i - \boldsymbol{k}_f$ and $\omega = \hbar(k_i^2 - k_f^2)/(2m)$. Here, $\boldsymbol{G}_m$ is a magnetic reciprocal-lattice vector, $\boldsymbol{q}$ is the relative momentum transfer, and $\boldsymbol{k}_{i,f}$ are the incident and final neutron wave vectors. $S(\boldsymbol{q}, \omega)$ is related to the imaginary part of the generalized magnetic susceptibility via

$$S(\boldsymbol{q}, \omega) = \frac{\chi''(\boldsymbol{q}, \omega)}{1 - \exp(-\hbar\omega/k_B T)}. \quad (1)$$

The real and imaginary parts of the generalized susceptibility $\chi(\boldsymbol{q}, \omega)$ are Kramers-Kronig related. A general form of $\chi''(\boldsymbol{q}, \omega)$ is given by $\chi''(\boldsymbol{q}, \omega) = \chi'(\boldsymbol{q})F(\omega)\omega$, where $\chi'(\boldsymbol{q})$ is the real part of the static susceptibility and $F(\omega)$ is the spectral weight function, which is an even function of ω and satisfies the normalization condition $\int_{-\infty}^{\infty} F(\omega)d\omega = 1$. Above the ordering temperature, spin fluctuations at small $\boldsymbol{q}$ are strongly damped and the spectral-weight function takes on a Lorentzian shape [21]:

$$F(\omega) = \frac{1}{\pi}\frac{\Gamma}{\Gamma^2 + \omega^2}. \quad (2)$$

To extract the inverse of the magnetic correlation length κ from Q scans, we use the following Lorentzian form for the

static susceptibility [4]:

$$\chi'(\boldsymbol{q}) = \frac{\chi'(\mathbf{0})}{1 + q^2/\kappa^2}, \tag{3}$$

where $\chi'(\mathbf{0}) \equiv \chi_0$ corresponds to the staggered magnetic susceptibility. The Kramers-Kronig relation connects $\chi'(\boldsymbol{q})$ and $S(\boldsymbol{q}, \omega)$ via

$$\begin{aligned} k_B T \chi'(\boldsymbol{q}) &= \int_{-\infty}^{\infty} \frac{1 - \exp(-\hbar\omega/k_B T)}{\hbar\omega/k_B T} S(\boldsymbol{q}, \omega)\, d(\hbar\omega) \\ &\simeq \int_{-\infty}^{\infty} S(\boldsymbol{q}, \omega)\, d(\hbar\omega) = S(\boldsymbol{q}), \end{aligned} \tag{4}$$

where $\hbar\omega \ll k_B T$ was assumed [21,61]. Hence, $S(0) \propto \chi_0 T$ follows for the static case at $\boldsymbol{q} = 0$. To determine S($\boldsymbol{q}$), in principle, it would be required to measure the entire S($\mathbf{q}, \omega$) function and perform a numerical ω integration, which can be avoided in 2D systems by using an energy integrating TAS configuration, as introduced by Birgeneau *et al.* [62]. In this configuration the TAS analyzer is removed (two-axis mode) and k_f is aligned perpendicular to the 2D layers, corresponding to the *ab* plane in Ca_2RuO_4. The magnitude of k_f varies with ω, but the relevant components of $\boldsymbol{q}$ in the 2D planes are constant and independent of ω. In consequence, the detector signal corresponds to an energy integration with lower integration limit (energy-gain scattering) given by the thermal energy of the fluctuations, and upper limit (energy-loss scattering) given by the energy E_i of the incident neutrons:

$$S(\boldsymbol{q}) = \int_{-\infty}^{\infty} S(\boldsymbol{q}, \omega)\, d(\hbar\omega) \approx \int_{-k_B T}^{E_i} S(\boldsymbol{q}, \omega)\, d(\hbar\omega). \tag{5}$$

In the case of Ca_2RuO_4, we achieved this energy-integrating configuration with $k_f \parallel c$ by choosing $Q = (1\,0\,0.83)$ for $k_i = 1.75\,\text{Å}^{-1}$. For $Ca_3Ru_2O_7$, due to the 3D character of the AFM order [55], the ideal energy-integration configuration with $k_f \parallel c$ can in principle not be obtained, as Q_L cannot be chosen arbitrarily. However, as discussed in Appendix A, the effect of this imperfect energy integration on the measured linewidth κ in the two-axis configuration (without analyzer) is insignificant for our determination of the critical exponent ν. Thus, the two-axis data of $Ca_3Ru_2O_7$ were not corrected for the integration effect.

III. RESULTS

A. Static critical properties of Ca_2RuO_4

In Ca_2RuO_4, the magnetic moments point along the *b* axis of the orthorhombic unit cell [45] [Fig. 1(a)] with a possible small canting in the *c* direction ($m_c \approx 0.1 m_b$) [63]. The magnetic susceptibility in the paramagnetic state indicates quasi-2D spin fluctuations [64], which was recently also found from the magnon dispersion in the ordered phase [50], where the following parameters were derived: $J = 5.8\,\text{meV}$, $J_{XY} = 0.87\,\text{meV}$ for the Heisenberg and *XY*-type exchange couplings and $E = 25\,\text{meV}$, $\epsilon = 4\,\text{meV}$ for the single-ion terms of the tetragonal and orthorhombic symmetries, respectively. An interlayer coupling J' was not required to describe the magnon dispersion [50], which is in line with studies on 1% Ti-doped Ca_2RuO_4, where a very small $J' = 0.03\,\text{meV}$ was reported [65]. Hence, the strong tetragonal term *E* and the small *J*0 signal that Ca_2RuO_4 can be regarded as a quasi-2D *XY* AFM.

In the following TAS measurements on Ca_2RuO_4, we use the energy-integrating two-axis mode (see Methods and Ref. [62]), which can be applied due to the 2D character of the magnetism, with critical fluctuations that are expected to be independent of Q_L. We perform Q_H scans around $Q = (1\,0\,0.83)$, which lies on the rod of the 2D magnetic scattering intensity. This corresponds to an energy-integrating configuration with alignment of $k_f \parallel c$ at $Q = (1\,0\,0.83)$ for $k_i = 1.75\,\text{Å}^{-1}$. Moreover, the advantage of a momentum Q that is slightly off from a magnetic Bragg peak position is that the signatures of critical scattering can be particularly pronounced [66]. Accordingly, we observe an enhancement of the scattered intensity at $Q = (1\,0\,0.83)$ [inset in Fig. 1(b)] for temperatures in the vicinity of the anticipated T_N of approximately 110 K [45,64]. More specifically, we observe that the critical scattering intensity peaks at a temperature slightly higher than 110 K. This behavior is likely related to the fact that T_N of our Ca_2RuO_4 sample is not sharply defined, but a distribution of Néel temperatures is present [see gray shaded area in Fig. 1(b)], in spite of the confirmed excellent crystalline quality (see Methods and Ref. [50]). This variance of T_N likely results from microstrains within the crystal, which emerge below the concomitant structural and metal-to-insulator transition at 360 K [46] and could be reminiscent of the (pseudo)spin-lattice coupling in Sr_2IrO_4 [67,68]. In the following analysis, we take this distribution of T_N into account, which allows us to extract the critical properties of Ca_2RuO_4 similarly to the case of a sharply defined T_N.

For an ideal second-order phase transition, the order parameter (staggered magnetization *M*) is $I \propto M^2 \propto |t|^{2\beta}$ and vanishes above T_N. Thus, the critical exponent β can be determined from the measured nominal magnetic (1 0 0) peak intensity I_{100} in Fig. 1(b). In general, β and the other critical exponents are extracted from the slopes of linear fits in double-logarithmic plots (see $Ca_3Ru_2O_7$ below). However, due to the present variance of T_N, the data in Fig. 1(b) cannot be described directly with the PL scaling function. Note that especially the intensity around 110 K does not show the expected sharp drop but is smeared out. This rounding of the intensity evolution cannot be attributed to critical scattering above T_N, since the data in the inset of Fig. 1(b) indicate that the critical contribution is two orders of magnitude smaller. Thus, we fit the (1 0 0) data in the range 90–120 K ($-0.2 < t < 0.1$) with a convolution of the above-mentioned PL and a Gaussian distribution of T_N with full width at half maximum (FWHM) ΔT_N [Fig. 1(b)]. The resulting fit parameters are $T_N = 112.20(1)\,\text{K}$, $\Delta T_N = 4.84(1)\,\text{K}$, and $\beta = 0.158(6)$. The β value lies in between the limits of the 2D Ising (2D-I) ($\beta = 0.125$ [4]) and 2D *XY* model ($\beta = 0.23$ [69,70]), as suggested for a *XY* system with fourfold crystal-field anisotropy (*XYh*$_4$) [71]. Figure 1(c) shows I_{100} and the fit curve on a double-logarithmic scale, illustrating that the PL fit provides an adequate description of the data below T_N, and also for a range of temperatures above T_N. Note that the strong deviation from a simple PL (straight line in double-logarithmic plot) is due to the Gaussian distribution of T_N.

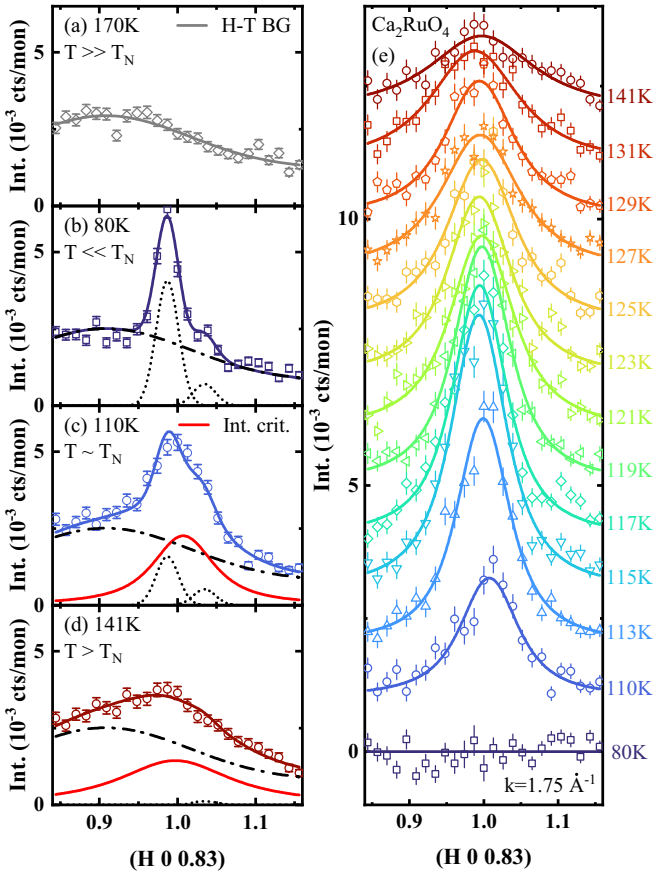

FIG. 2. Selected energy-integrated Q_H scans around (H 0 0.83) for Ca_2RuO_4 before (a–d) and after (e) background (BG) subtraction. The data contain a T-independent constant BG, which was determined at $T = 170$ K and labeled as "high-temperature" (H-T) BG (a). Panels (b)–(d) show the H-T BG as a dash-dotted line. At low T, two small T-dependent resolution-limited Gaussian peaks (black dotted lines) appear (b–d), which are attributed to the magnetic (1 0 1) peak of the main domain and the (0 1 1) peak of the twin domain, respectively. The critical scattering component (Voigt profile) is shown as a red line. (e) Selected Q_H scans after BG subtraction with corresponding fit functions (solid lines). For clarity the data are plotted with a constant offset.

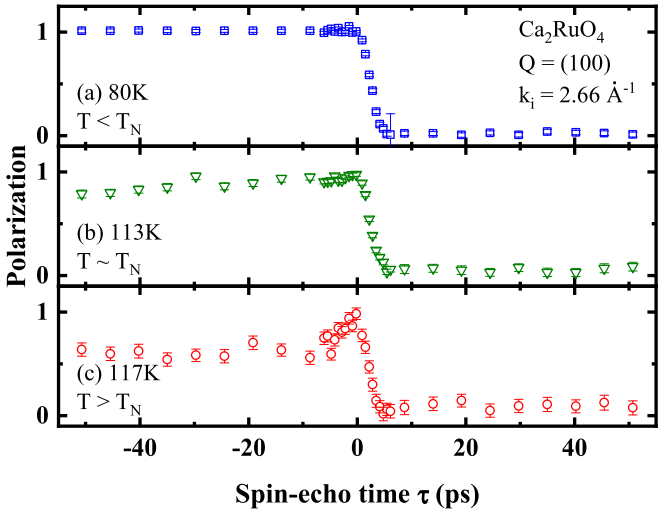

FIG. 3. NSE polarization vs spin-echo time τ at $Q = (1\,0\,0)$ for selected temperatures. According to Ref. [78], we define $\tau < 0$ for measurements in spin-echo configuration, i.e., with antiparallel magnetic fields $\boldsymbol{B}_0$ in the spin-echo arms, and $\tau > 0$ for measurements in Larmor-diffraction mode, i.e., with parallel magnetic fields in the spin-echo arms. The lack of a significant polarization at $\tau > 0$ and the absence of oscillations of the polarization at small τ [78] imply that the contribution of transverse fluctuations along the c axis to the signal is marginal.

As a next step we perform Q_H scans around (1 0 0.83) to determine the inverse correlation length $\kappa(T)$ (Fig. 2). Prior to fitting of the scans with Voigt profiles, we thoroughly determine the background (BG) contributions. Representative scans are shown in Fig. 2(a)–2(d). We identify several components of the BG.

(i) A temperature-independent component is determined at 170 K [Fig. 2(a)], i.e., well above T_N. The obtained fit (H-T BG) is employed as BG in the analysis of the data measured at all other temperatures [see dash-dotted lines in Figs. 2(a)–2(d)].

(ii) The scan at the lowest measured temperature $T = 80$ K [Fig. 2(b)] shows two incommensurate peaks besides the H-T BG.

By comparing the temperature-dependent intensity of these resolution-limited peaks with the intensities of the magnetic (1 0 0) [Fig. 1(c)] and (1 0 1) peaks [45], they can be assigned to the (1 0 1) peak of the main domain, and the (0 1 1) peak of the twin domain [63]. The (1 0 1) peak is likely associated with a "B-centered" phase with a different propagation vector and transition temperature $T_{N,101} \approx 150$ K [45]. Finally, we subtract the H-T BG and the aforementioned two peaks with proper T scaling from the Q scans and obtain the corrected data shown in Fig. 2(e). These data are well described by Voigt profiles, which correspond to the convolution of the intrinsic Lorentzian with half width at half maximum (HWHM) κ [Eq. (3)] and the Gaussian instrumental resolution. The constant width of the instrumental Gaussian (FWHM ≈0.034 r.l.u.) was extracted from the 80-K scan in agreement with simulations carried out with the RESLIB [72] and TAKIN [73] softwares, respectively. Prior to the discussion of the inverse correlation length κ extracted from Fig. 2(e), we address the possible presence of concomitant longitudinal and transverse fluctuations. In general, critical longitudinal (parallel to the static ordering vector) and noncritical transverse fluctuations are expected to be both visible and not separated for all measurement configurations used in this paper. However, NSE spectroscopy [74–77] is capable to separate the two components [78]. To this end, we carried out high-resolution NSE measurements on Ca_2RuO_4 at TRISP (see Methods), at $Q = (1\,0\,0)$ with $k_i = 2.66\,\text{Å}^{-1}$. Figure 3 shows the resulting spin-echo polarization vs the spin-echo time $\tau \equiv (m^2\omega_L L)/(\hbar^2 k_i^3)$ for selected temperatures, with the Larmor frequency $\omega_L = \gamma_n \boldsymbol{B}_0$ ($\gamma_n = 2.916$ kHz/Oe) corresponding to the static magnetic fields $\boldsymbol{B}_0$ in the spin-echo arms with length L. A high-temperature BG (170 K) was subtracted from the data. According to Ref. [78], possible transverse fluctuations in Ca_2RuO_4 (along the c axis) would lead to a polarized signal for $\tau > 0$, i.e., for parallel magnetic fields $\boldsymbol{B}_0$. Conversely,

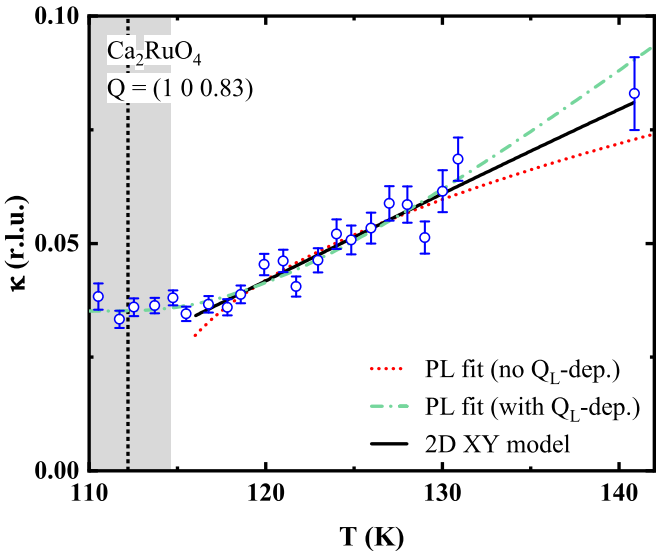

FIG. 4. Inverse correlation length $\kappa(T)$ of Ca_2RuO_4 with various fit functions: The green dash-dotted line is a PL fit with $\nu = 1.0(1)$ and $\kappa_{3D} = Q_L\sqrt{J'/J} = 0.035(1)$. The red dashed line is a PL fit for $T > 116\,\mathrm{K}$ and $\kappa(T \leqslant T_N) = 0$, with $\nu = 0.42(4)$. The black solid line corresponds to a 2D XY fit for $T > 116\,\mathrm{K}$, with $T_{KT} = 87(2)\,\mathrm{K}$ and $b = 1.9$. The vertical dashed line shows the average T_N and the gray bar shows the variance of T_N.

longitudinal fluctuations (along the b axis) lead to a polarized signal for $\tau < 0$. Figure 3 shows a significant polarization at $\tau < 0$ that depolarizes as a function of τ and T, respectively, indicative for the T-dependent linewidth $\Gamma(T)$ of the critical fluctuations. By contrast, no significant polarization at $\tau > 0$ was measured. Moreover, no oscillations of the polarization at small τ were observed, which are a hallmark of interference effects between transverse and longitudinal fluctuations [78]. Hence, we conclude that transverse fluctuations along the c axis are negligible or absent in Ca_2RuO_4 and we assume in the following that the fluctuations observed in the TAS experiments are also purely longitudinal. A possible explanation for this absence is that these fluctuations are gapped and thus not excited in the T range of our paper.

The inverse correlation length $\kappa(T)$ resulting from the fits in Fig. 2 is shown in Fig. 4. Notably, a T-dependent broadening above 116 K ($T_N + 4\,\mathrm{K}$) can be observed, while the Q width is approximately constant for $T < 116\,\mathrm{K}$. This is in contrast to the conventional critical scaling theory where κ should converge to zero at T_N. In the following we will discuss several models to explain this saturation of κ at $T < 116\,\mathrm{K}$.

(i) An obvious reason for such lower bound of the linewidth is crystallographic defects [79,80]. One possible type of defect in Ca_2RuO_4 can be domain walls of the structural twins, which can disrupt the long-range magnetic ordering. However, from the Q width of the (1 0 0) magnetic peak (not shown here) we derive a domain size of $>300\,\text{Å}$, which is much larger than the extracted correlation length of 20 Å at $Q = (1\,0\,0.83)$ and $T = 110\,K$. Thus we exclude domain size effects as the origin of the observed linewidth saturation.

(ii) At $T \simeq T_N$, i.e., close to the 3D ordering, one expects a crossover of the critical fluctuations from a 2D to a 3D character with an increasing influence of the Q_L component on κ. This effect was described in Refs. [17,81] and modeled by an effective κ with $\kappa_{eff}^2 = \kappa_{3D}^2 + \kappa_{pow}^2$, $\kappa_{3D}^2 \equiv Q_L^2 J'/J$, and $\kappa_{pow}^2 \equiv \kappa_0 t^{2\nu}$. A fit of our experimental $\kappa(T)$ with a convolution of κ_{eff} and the aforementioned Gaussian distribution of T_N results in an exponent $\nu = 1.0(1)$ and $\kappa_{3D} = 0.035(1)$, and describes the data over the entire measured T range (green dash-dotted line in Fig. 4). The exponent ν matches the universal value of the 2D-I model ($\nu_{2DI} = 1$ [4]). From $\kappa_{3D} = 0.035(1)$ we obtain the ratio $J'/J = 0.002$. This is in agreement with $J'/J = 0.004$ derived from INS on 1% Ti-doped Ca_2RuO_4 [65]. Assuming $J = 5.8\,\mathrm{meV}$ [50], this corresponds to an interlayer coupling $J' \approx 0.01\,\mathrm{meV}$.

The red dashed line in Fig. 4 shows a PL fit $\kappa \propto |t|^\nu$ without a κ offset at T_N, i.e., without a Q_L dependence due to 3D correlations, convoluted with the variance of T_N. Only the data for $T > 116\,\mathrm{K}$, i.e., beyond the saturation region, were included in the fit. The rounded shape of the red line towards T_N results from the T_N variance. The resulting $\nu = 0.42(4)$ is close to the mean-field (MF) value of $\nu_{MF} = 0.5$, but is at odds with $\nu = 1.0(1)$ obtained in the previous PL fit with the offset in κ, although both fits give a satisfactory description of the data for $T > 116\,K$. Furthermore, we note that a fit of $\kappa(T)$ with a 2D quantum Heisenberg model [82–84] with an anisotropy parameter accounting for 3D correlations close to T_N [31] also gives a good agreement with the data, but we exclude this model due to the large easy-plane anisotropy in Ca_2RuO_4.

We now focus on the 2D XY model, which was already suggested in the context of the magnon dispersion [50] and describes a topological phase transition accompanied by an unbinding of vortex/antivortex pairs [9–11]. The parameters of this model are the Kosterlitz-Thouless (KT) temperature T_{KT}, a critical exponent $\eta = 0.25$, and a dimensionless nonuniversal parameter b [11,85], which was previously determined to be approximately 1.9 [81]. The correlation length in this model is defined as [11]

$$\xi \propto \exp\left(\frac{b}{\sqrt{t_{KT}}}\right), \quad \text{with } t_{KT} \equiv (T/T_{KT} - 1). \tag{6}$$

For systems with magnetic long-range order the actual KT transition at $T_{KT} < T_N$ is usually obscured by the 3D ordering with nonzero interlayer couplings J', which set in around T_N. The relation between T_{KT} and T_N is given by [69,81]

$$\frac{T_N - T_{KT}}{T_{KT}} = \frac{4b^2}{[\ln(J/J')]^2}. \tag{7}$$

Assuming $J'/J = 0.002$, as derived from the above PL fit with Q_L dependence to capture the κ offset, we obtain $\tilde{T}_{KT} = 82\,\mathrm{K}$, with $\tilde{T}_{KT}$ denoting the KT temperature derived from Eq. (7) and T_{KT} the KT temperature extracted from fits to $\kappa(T)$ in the following. As expected for a system with a KT temperature below T_N, our data do not show any signatures of a transition around 82 K. Nonetheless, we use this model in the following to describe the scaling above T_N, as it was demonstrated [86–88] and experimentally confirmed [16,17,89], that even a XY anisotropy much weaker than in the case of Ca_2RuO_4 can result in 2D XY scaling. Hence, as a next step, we fit Eq. (6) to $\kappa(T)$ for $T > 116\,\mathrm{K}$. Note that T_{KT} is much lower than the

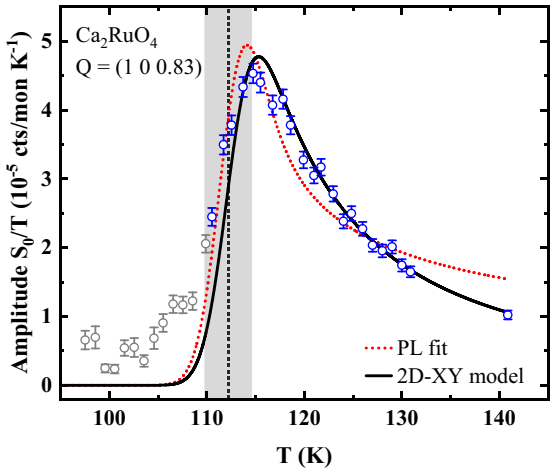

FIG. 5. Peak amplitude $S_0(T)/T$ of Ca_2RuO_4. The red dotted line is a PL scaling fit [$\gamma = 0.47(2)$] and the black solid line corresponds to the 2D XY model. The gray data points were not included in the fit. The black vertical line indicates T_N and the gray bar indicates the variance of T_N.

lower limit of the fitting range, i.e., a possible distribution of T_N and KT temperatures in the sample will not affect the result of the fit significantly and is therefore not considered here. The resulting fit (solid black line in Fig. 4) with $T_{KT} = 87(2)\,K \approx 0.8T_N$ provides an excellent description of the data, and is in reasonable agreement with $\tilde{T}_{KT} = 82\,K$ from Eq. (7). We note that a fit with b as a free parameter did not converge, since it couples strongly to T_{KT}. Thus, b was fixed to 1.9 [81]. We also note that η was fixed to 0.25 [10], although η can deviate from this value in specific models on critical scattering, which then would affect the line shape of $\chi'(\boldsymbol{q})$ from the Lorentzian form employed in this paper (see Methods). However, we find that in our case the deviation of the line shape for $\eta = 0.25$ is relatively subtle (see Appendix E) and lies below the detection threshold of the statistics of our data. Therefore, we use the simplest approach for $\chi'(\boldsymbol{q})$ in the present paper, which is the Lorentzian function.

In summary, the data in Fig. 4 are consistent with both the 2D XY (black solid line) and 2D-I (green dash-dotted line) scaling behavior for $T > 116\,K$. Nevertheless, we rule out the latter scaling for the description of $\kappa(T)$, as the critical peak amplitudes $S_0(T)/T$ (Fig. 5) with the corresponding critical exponent γ (see below) are not compatible with the 2D-I model, although a crossover to 2D-I scaling close to T_N is expected due to the orthorhombic anisotropy ϵ [50]. While this crossover from 2D XY to 2D-I scaling presumably occurs in a T range very close to T_N and is not resolved in our data, we attribute the observed saturation for $T < 116\,K$ to a crossover to 3D coupling, which eventually drives the magnetic transition. In addition to $\kappa(T)$, we analyzed the staggered susceptibility χ_0, which also shows critical behavior close to T_N. Related via the Kramers-Kronig relation, χ_0 is proportional to $S(0) \propto \chi_0 T$ (see Methods), i.e., the peak amplitude of the Lorentzian profile $S(q)$. In the following, $S(0)$ will be denoted as S_0. Figure 5 shows the temperature dependence of the amplitude measured at (1 0 0.83). First, we fit a PL $\propto |t|^{-\gamma}$ in the range $110 < T < 140\,K$, convoluted with the Gaussian T_N distribution by assuming $S_0 = 0$ for $T < T_N$. The agreement with the data is not convincing and the extracted critical exponent $\gamma = 0.47(2)$ does not match universal values [4], especially not the value predicted for the 2D-I model ($\gamma_{2DI} = 1.75$). Furthermore, since scaling theory predicts PL behavior for temperatures both above and below T_N, we also carried out a fit over the entire T range (see Appendix B). Nevertheless, such fit yields a similar value for γ, corroborating that PL scaling is not suitable to capture the temperature dependence of the amplitudes. Next, we fit the range $110 < T < 140\,K$ with the 2D XY model by using the scaling relation $\chi_0 \propto \xi^{2-\eta}$ [11]:

$$\frac{S(0)}{T} \propto \exp\left(\frac{B}{\sqrt{t_{KT}}}\right), \tag{8}$$

with $B \equiv b(2-\eta)$ and $T_{KT} = 87\,K$ from above. We fixed $\eta = 0.25$ as suggested for the 2D XY model [11]. The model gives a good description of the data with only one free parameter in the fit, that is, the proportionality constant in Eq. (8).

B. Static critical properties of $Ca_3Ru_2O_7$

$Ca_3Ru_2O_7$ exhibits FM bilayers [Fig. 1(d)], which are stacked in an AFM fashion along the c axis (A-type AFM) [51,52]. From the magnon dispersion in the ordered phase [54,55] the following terms of the Hamiltonian were derived: $J = -3.75\,meV$, $J_c = -6.5\,meV$ for the nearest-neighbor and intrabilayer coupling and $E = 5.5\,meV$, $\epsilon = 2.5\,meV$ for the tetragonal and orthorhombic anisotropy, respectively. Notably, the magnon dispersion along the c direction and interbilayer coupling J' are very small or absent [54,55]. Hence, $Ca_3Ru_2O_7$ exhibits an easy-plane anisotropy E and strongly coupled bilayers (large J_c) that can possibly act as one magnetic entity [90], suggesting that $Ca_3Ru_2O_7$ could also be a candidate for quasi-2D XY critical behavior. This calls for an investigation whether the critical behavior in the bilayer compound $Ca_3Ru_2O_7$ falls either into the quasi-2D or the 3D limit, or corresponds to an intermediate case.

Figure 1(e) shows the magnetic (0 0 1) peak intensity I_{001} measured upon warming, with a first-order transition at $T_{N,2} \approx 48\,K$ and a second-order transition at $T_{N,1} \approx 56\,K$, in good agreement with Ref. [91]. In contrast to the magnetic peak of Ca_2RuO_4 [Fig. 1(c)], I_{001} of $Ca_3Ru_2O_7$ drops sharply towards $T_{N,1}$, suggesting that possible distribution of Néel temperatures $\Delta T_{N,1}$ is negligible. We explain this observation with the appearance of less pronounced intrinsic crystal strains above the structural transition at $T_{N,2}$. Moreover, in comparison to Ca_2RuO_4, the crystal-field distortions are expected to be weaker in $Ca_3Ru_2O_7$ [55]. In order to establish the presence of critical scattering we measure the scattering intensity in distance to the (0 0 1) Bragg position at $Q = (0\,0\,1.3)$ as a function of temperature [see inset Fig. 1(e)]. Notably, the critical intensity in the inset in Fig. 1(e) peaks at $T_{N,1}$ and its magnitude is compatible with the remaining intensity for $T > T_{N,1}$ in Fig. 1(e). A PL fit (without a $T_{N,1}$ distribution) in the range $49\,K < T < T_{N,1}$ ($0 < |t| < 0.1$), i.e., between $T_{N,1}$ and $T_{N,2}$, yields a critical exponent $\beta = 0.230(6)$ and $T_{N,1} = 54.16(2)\,K$ [Figs. 1(e) and 1(f)]. Figure 1(f) shows I_{001} and the PL fit on a double-logarithmic scale, suggesting a purely linear evolution of I_{001} in such a plot for the measured

temperatures. The obtained value of β matches the universal value of the 2D XY model ($\beta = 0.23$ [69,70]), although it should be taken with caution as the point density in close vicinity of $T_{N,1}$ is sparse. Moreover, the intrinsic scaling behavior could be obfuscated due to a contribution in the scattering intensity from an overlap with the second transition at $T_{N,2}$.

To extract $\kappa(T)$ and the amplitude of the critical scattering, we carried out Q_H scans around (H 0 1) in the two-axis mode. The ideal energy-integrating configuration used for Ca_2RuO_4 is not applicable for 3D systems (see Methods). However, a numerical simulation confirmed that the integration according to Eq. (5) is sufficiently satisfied for our two-axis configuration in $Ca_3Ru_2O_7$ (see Appendix A). Furthermore, we note that for $Ca_3Ru_2O_7$ spin-echo experiments to discern longitudinal and transverse fluctuations have not been carried out. Nonetheless, from the fact that in the present paper both the static and dynamical critical fluctuations in $Ca_3Ru_2O_7$ are well captured by power laws (see below), we conclude that the noncritical transverse fluctuations do not contribute significant intensity around $T_{N,1}$ [66]. From the Q_H scans we subtracted two BG components.

(i) The first is a sharp peak at $H = 0$, which is clearly visible at high T (150 K) [Fig. 6(a)]. In addition, we performed a scan around (H 0 1.25) at 100 K and found that the sharp feature is independent of Q_L and T (see Appendix C). Thus, we assign it to 2D diffuse nuclear scattering from disorder along the c axis due to, e.g., stacking faults.

(ii) The second is a sharp resolution-limited (0 0 1) peak with Gaussian width ≈0.01 r.l.u. [Fig. 6(b)], which rapidly vanishes above $T_{N,1}$. The (0 0 1) peak is intense at $T \leqslant 54.5$ K and the extraction of critical scattering is not reliable. The BG corrected Q_H scans can be captured by a Voigt profile (intrinsic Lorentzian critical scattering convoluted with instrumental Gaussian profile) [Fig. 6(e)]. A critical scattering intensity can be clearly observed at least up to 70 K. We note that there might be a contribution from critical fluctuations even at 100 K, but since it is very weak we do not consider this temperature in the following analysis.

The resulting Q width $\kappa(T)$ is plotted in Fig. 7 on double-logarithmic scales. Note that in the following analysis of $Ca_3Ru_2O_7$, we extract the critical exponents of the PLs from the slopes of linear fits in plots with double-logarithmic scaling, whereas plots with linear scaling were employed in the above analysis of Ca_2RuO_4 (Figs. 4 and 5), due to the variance of T_N in the latter material. The red dotted line is a linear fit in the range $55 \leqslant T \leqslant 70$ K with the slope corresponding to the critical exponent in the scaling relation $\kappa \propto t^{\nu}$. The obtained $\nu = 0.550(4)$ lies between the values predicted for the 3D-I ($\nu_{3DI} = 0.630$ [6]) and the MF model ($\nu_{MF} = 0.5$ [4]). The MF model, however, is at odds with the modeling of the magnon dispersion of $Ca_3Ru_2O_7$ in Ref. [55], which used only nearest-neighbor couplings and no long-ranged interactions in the spin Hamiltonian [4]. Thus, we assign the critical scaling of $\kappa(T)$ rather to the 3D-I model (green solid line in Fig. 7), which also captures the data well. In analogy to Ca_2RuO_4, we also fit $\kappa(T)$ of $Ca_3Ru_2O_7$ with the 2D XY model, using Eq. (6), $\eta = 0.25$, and $b = 1.9$. The obtained KT temperature is $T_{KT} = 45.42(6)$ K, but the agreement between the fit (black dash-dotted) and the data is unsatisfactory for most temperatures (Fig. 7). We also test a fit with b as a free parameter, since lower values of b were reported in some experiments [92,93] and derived in numerical calculations [85]. Such a fit (not shown here), with $b = 0.44(1)$ and $T_{KT} = 53.18(7)$, yields a better agreement with the $\kappa(T)$ data of $Ca_3Ru_2O_7$. However, using the latter values of b and T_{KT} as an input for the fit of the critical amplitudes (see below) results in a very strong deviation from the data (not shown here) and is therefore disregarded. In summary, we conclude that the 3D-I model is most appropriate to describe the critical behavior of $\kappa(T)$ above T_N.

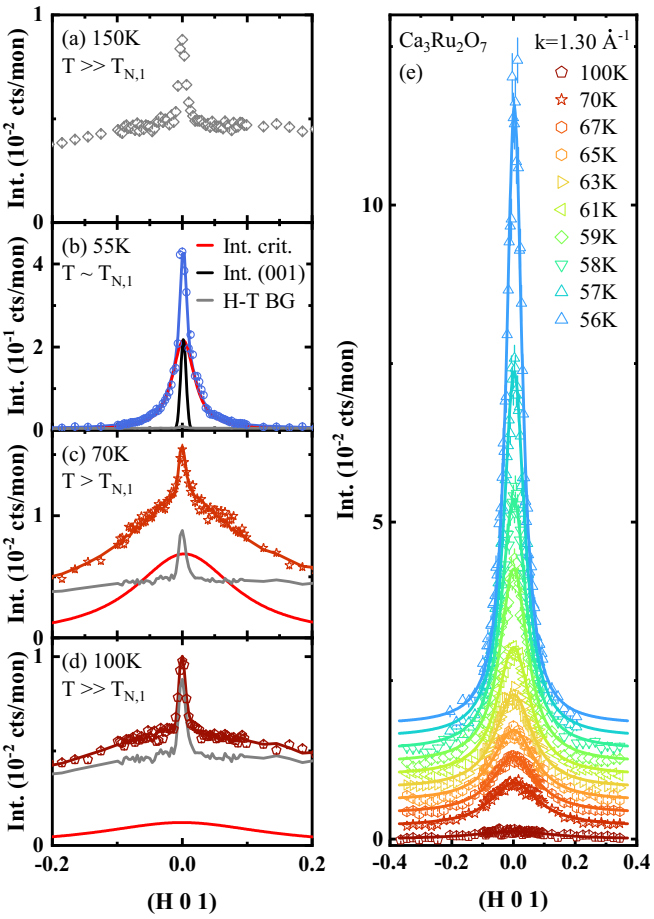

FIG. 6. Selected energy-integrated transverse Q_H scans around (H 0 1) for $Ca_3Ru_2O_7$ before (a–d) and after (e) BG subtraction. (a) The high-T BG contains a sharp peak that is independent of Q_L. (b) Close to $T_{N,1}$, a resolution-limited Gaussian component arising from the (0 0 1) magnetic Bragg peak is observed in addition to the Voigt profile of the critical scattering. (c, d) Above $T_{N,1}$, the sharp peak and critical scattering are observed. (e) Selected Q_H scans after BG subtraction with corresponding fits (solid lines). For clarity the data are plotted with a constant offset.

The critical exponent γ of the staggered susceptibility is obtained by fitting the corresponding peak amplitudes S_0/T with the PL scaling $\chi \propto t^{-\gamma}$ in the range $55 \leqslant T \leqslant 70$ K. From the slope of the corresponding linear fit (red dotted line) in the double-logarithmic plot (Fig. 8), we extract $\gamma = 1.290(4)$, which is close to the value predicted for the 3D-I model ($\gamma_{3DI} = 1.238$ [6]), as indicated by the green solid line in Fig. 8. For the comparison with the 2D XY model,

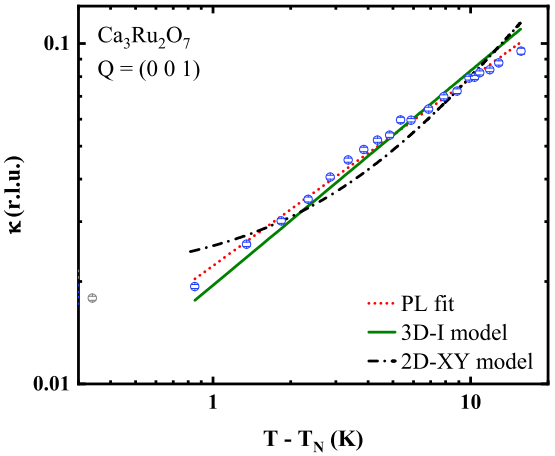

FIG. 7. Inverse correlation length $\kappa(T)$ of $Ca_3Ru_2O_7$ on double-logarithmic scales. The red dotted line is a linear fit in the range $55 \leqslant T \leqslant 70$ K, with the slope corresponding to the critical exponent $\nu = 0.550(4)$, according to the scaling relation $\kappa \propto t^{\nu}$. The green solid line indicates 3D-I scaling. The black dash-dotted line corresponds to the 2D XY model with $T_{KT} = 45.42(6)$ K and $b = 1.9$. The gray data point was not included in the fit.

we use Eq. (8), with $\eta = 0.25$ and $b = 1.9$, as well as $T_{KT} = 45.42$ K determined from the fit of $\kappa(T)$ above. In spite of a good agreement with the data at $T > T_N + 2$ K (see black dash-dotted line), the PL fits are more suitable to describe the scaling of the critical amplitudes closer to T_N.

C. Dynamic critical properties of Ca_2RuO_4

Figures 9(a)–9(d) display selected energy scans at (1 0 0) measured on the cold neutron TAS FLEXX with $k_f = 1.3$ Å^{-1}. A T-independent BG from elastic incoherent scattering recorded at 170 K was subtracted from the raw data.

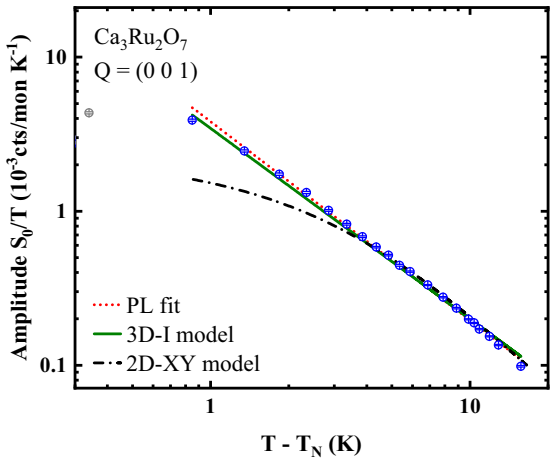

FIG. 8. Peak amplitude $S_0(T)/T$ of $Ca_3Ru_2O_7$ on double-logarithmic scales. The red dotted line is a linear fit with the slope corresponding to the critical exponent $\gamma = 1.290(4)$, according to the scaling relation $\chi \propto t^{-\gamma}$. The green solid line indicates 3D-I scaling. The black dash-dotted line corresponds to the 2D XY model with $T_{KT} = 45.42(6)$ K and $b = 1.9$. The gray data point was not included in the fit.

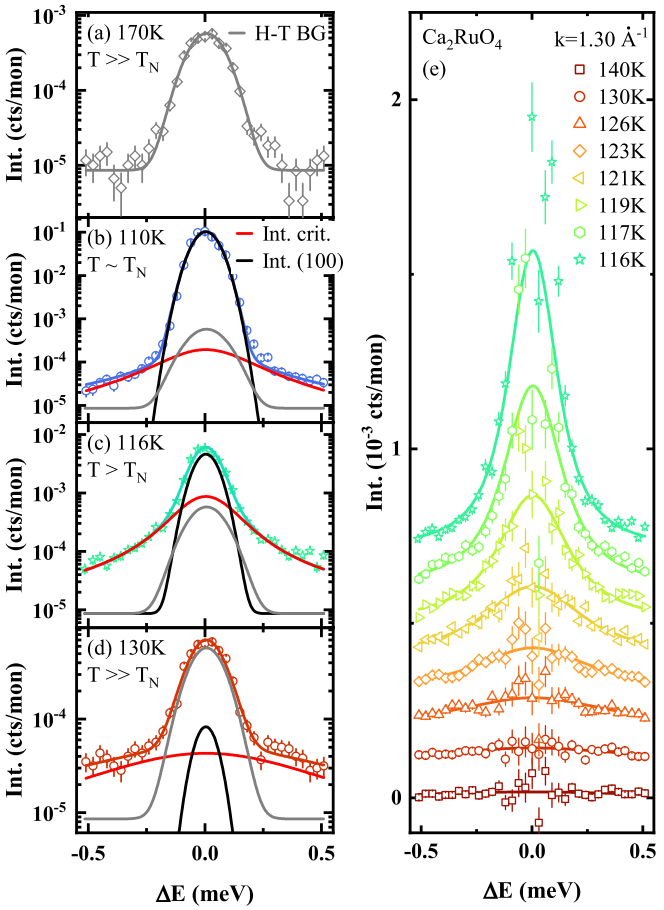

FIG. 9. Selected energy scans of Ca_2RuO_4 before (a–d) and after (e) BG subtraction. (a–d) Besides a constant high-T BG (170 K), we fitted a sum of a broad critical Voigt profile and a resolution-limited Gaussian peak over the entire T range. The latter is attributed to the magnetic (1 0 0) peak that shows the aforementioned distribution of T_N. (e) Selected energy scans after high-T BG and elastic (1 0 0) peak subtraction with corresponding fits (solid lines). For clarity the curves are plotted with a constant offset.

The BG corrected data are described by a fit with the sum of a resolution-limited Gaussian peak (FWHM ≈0.12 meV) and a Voigt function capturing the critical scattering. The resolution was extracted from the width of the elastic magnetic scattering well below T_N. The free parameters of the fits are the amplitude of the Gaussian peak, and the amplitude and width of the Voigt peak. The amplitudes of the Gaussian and the Voigt peaks match the intensities of the (1 0 0) peak [Fig. 1(b)] and the amplitude of the critical scattering at (1 0 0.83) [Fig. 1(b), inset] (see Appendix D). An overview of the energy scans and the resulting fit curves at selected temperatures is shown in Fig. 9(e). The resulting energy width $\Gamma(T)$ of the critical component is plotted in Fig. 10(a). Above 115 K the data show a significant broadening, while below no systematic trend was observed. For these data ($T \leqslant 115$ K) the intensity of the (1 0 0) peak is much stronger than the critical scattering and extraction of $\Gamma(T)$ in the fit is not reliable. Therefore, we exclude this T range in the following scaling analysis [gray data points in Fig. 10(a)]. To determine the dynamic critical exponent z from $\Gamma(T)$ above 115 K, in analogy to $\kappa(T)$, we fit

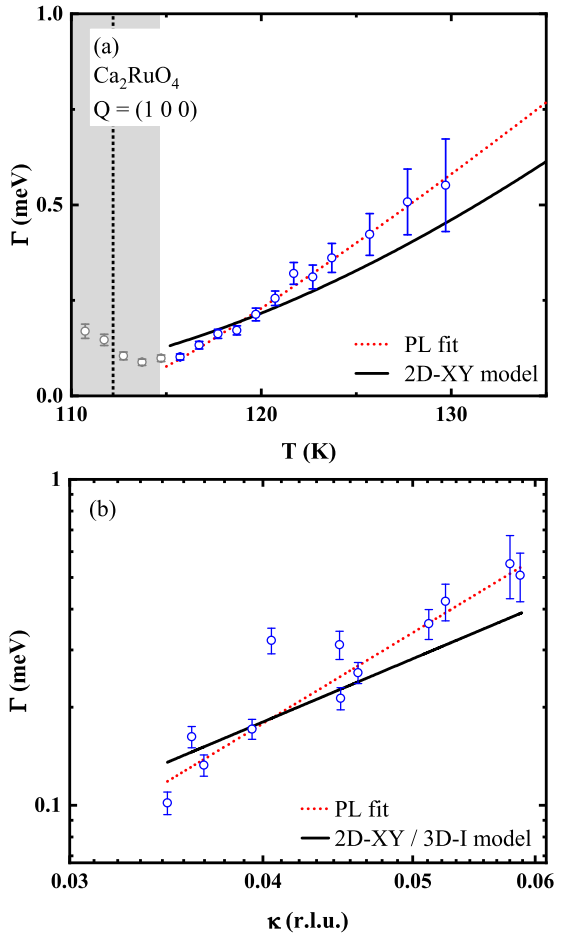

FIG. 10. (a) Energy width Γ of Ca_2RuO_4 vs temperature. The red dotted line is a PL scaling fit with exponent $z\nu = 1.1(1)$. The black solid line corresponds to a 2D XY scaling fit with $z_{XY} = 2.0$ [100]. The gray data points are not included in the fits. The black vertical line indicates T_N and the gray bar indicates the variance of T_N. (b) Energy width Γ of Ca_2RuO_4 vs the inverse correlation length κ on double-logarithmic scales. The red dotted line is a linear fit with the slope corresponding to the dynamical critical exponent $z = 2.9(2)$, according to the scaling relation $\Gamma \propto \kappa^z$. The black solid line corresponds to the 2D XY model with $z_{XY} = 2.0$ [100].

a convolution of the PL $\Gamma \propto |t|^{z\nu}$ with a Gaussian distribution of T_N (red dotted line). By assuming $\Gamma(T) = 0$ for $T \leqslant T_N$, as predicted by dynamic scaling theory [3], the PL fit yields $z\nu = 1.1(1)$. In spite of the good agreement with the data in Fig. 10(a), the error margin is relatively large and only the 3D-H model ($z\nu_{3DH} = 1.067$ [3,94]) and the 3D-I model ($z\nu_{3DI} = 1.26$ [3,6]) are reasonably close to the obtained exponent. However, 3D scaling is not expected well above T_N for this quasi-2D system. Furthermore, $z\nu = 1.1(1)$ is far away from 2D-I scaling ($z\nu_{2DI} = 1.75$ [4,95]), which was discussed in the context of $\kappa(T)$ of Ca_2RuO_4 (green dash-dotted line in Fig. 4).

Next, we examine the critical dynamics of Ca_2RuO_4 in terms of the 2D XY model. For the motion of vortices a dynamic scattering function $S(\boldsymbol{q}, \boldsymbol{\omega})$ with a quadratic Lorentzian form (central peak) was derived [85,96,97], and also experimentally observed [16,98,99]. However, such a central peak is not present in our data (Fig. 9), which can be captured by a simple Lorentzian function. Thus, we use instead the dynamic scaling relation $\Gamma \propto \kappa^z$, suggested to be appropriate for relaxational dynamics in the 2D XY model [100] to check for 2D XY scaling above 115 K. The black solid line in Fig. 10(a) shows the scaling for the critical exponent $z_{XY} = 2.0$, which was postulated for the 2D XY model [100]. The agreement with the data is not as good as for the PL fit, although at high temperatures the 2D XY scaling lies essentially within the error bars. The deviation at low temperatures could be due to the variance of T_N or a crossover to a different scaling behavior. We note that using z as a free fit parameter improves the agreement with the data, but the obtained value of $z_{XY} = 3.04(6)$ (fit not shown here) is at odds with the theory for the universality class.

In addition, we determine z directly from plotting Γ vs κ on double-logarithmic scales [Fig. 10(b)]. In such a plot, the slope of a linear fit to the data corresponds to the critical exponent of the scaling relation $\Gamma = \kappa^z$. The resulting dynamical critical exponent $z = 2.9(2)$ (red dashed line) is not compatible with any known universal value. Note, however, that the Γ vs κ data points in Fig. 10(b) were obtained by interpolation, as the Q and energy scans on Ca_2RuO_4 were taken at different Q positions and temperatures at two different instruments, which can lead to uncertainties. Specifically, the data points in Fig. 10(b) were generated by interpolating $\kappa(T)$ to the temperatures at which $\Gamma(T)$ was measured and the same fitting range ($T > 115$ K) was included, where the impact on the T_N distribution is negligible. Nevertheless, while the dynamical critical exponent of the linear fit deviates from a universal value, we find that the 2D XY model (solid black line) with the exponent $z = 2.0$ [100] captures the Γ vs κ data reasonably well [Fig. 10(b)].

D. Dynamic critical properties of $Ca_3Ru_2O_7$

Figures 11(a)–11(d) display selected energy scans at the (0 0 1) peak of $Ca_3Ru_2O_7$. A constant elastic incoherent high-T BG is subtracted from the energy scans, which was measured at $T = 100$ K, where the contribution of critical scattering is negligible [Fig. 6(d)]. Subsequently, a single Voigt function (Gaussian width ≈0.06 meV) is fitted to the scans. An overview of the energy scans after BG subtraction with the corresponding fits is plotted in Fig. 11(e) for selected temperatures.

The resulting energy width $\Gamma(T)$ of $Ca_3Ru_2O_7$ is shown in Fig. 12(a) on double-logarithmic scales. The data are well captured by a linear fit (red dotted line) in the range $55 \leqslant T \leqslant 70$ K with a slope $z\nu = 1.186(8)$, corresponding to the critical exponent in the scaling relation $\Gamma \propto t^{z\nu}$. This exponent is close to the value predicted for the 3D-I model ($z\nu_{3DI} = 1.260$ [3,6]) indicated by the green solid line in Fig. 12(a), which is consistent with the static critical properties. In analogy to Ca_2RuO_4, we also carry out a fit with the 2D XY model, using the dynamic scaling relation $\Gamma \propto \kappa^z$ with $z = 2.0$ [100]. The resulting fit [black dash-dotted line in Fig. 12(a)] describes the data reasonably well at high temperatures, but deviates strongly in proximity to T_N.

Figure 12(b) shows a plot of Γ vs κ on double-logarithmic scales, which allows us to determine z directly. From the

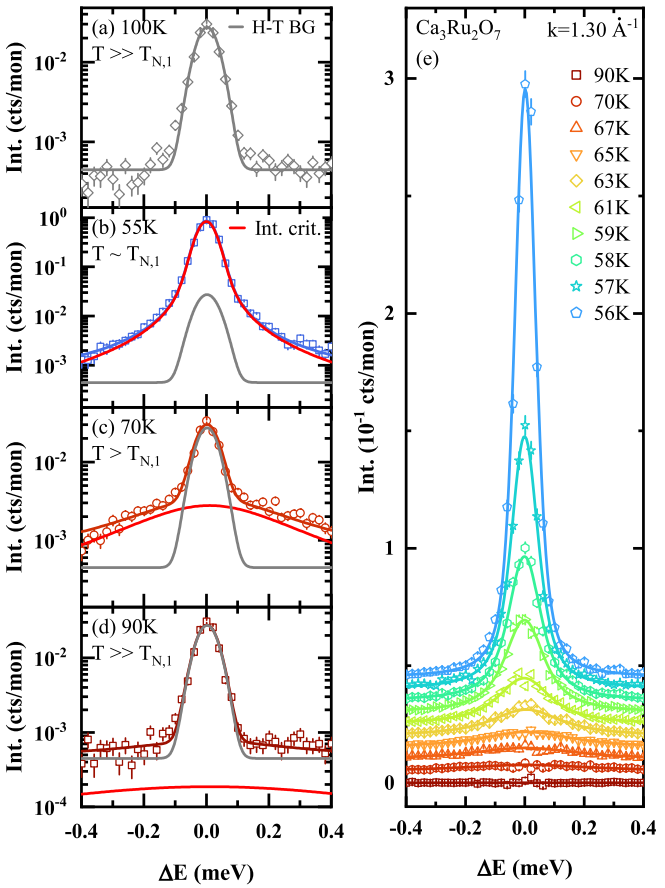

FIG. 11. Selected energy scans of $Ca_3Ru_2O_7$ before (a–d) and after (e) BG subtraction. (a–d) In contrast to Ca_2RuO_4, the $Ca_3Ru_2O_7$ data could be well fitted by a single Voigt profile and a constant elastic high-T BG measured at 100 K. (d) Selected energy scans after BG subtraction with corresponding fit functions (solid lines). For clarity the curves are plotted with a constant offset.

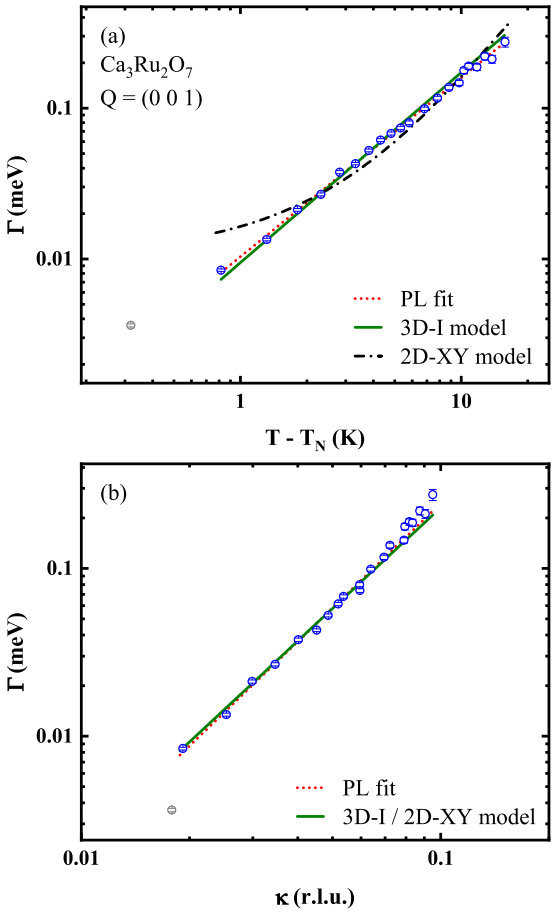

FIG. 12. Energy width Γ of $Ca_3Ru_2O_7$ vs temperature (a) and the inverse correlation length (b) on double-logarithmic scales. (a) The red dotted line is a linear fit with the slope corresponding to the critical exponent $z\nu = 1.186(8)$, according to the scaling relation $\Gamma \propto t^{z\nu}$. The green solid line indicates 3D-I scaling with $z\nu_{3DI} = 1.260$ [3,6]. The black dash-dotted line corresponds to the 2D XY model with the exponent $z = 2.0$ [100]. (b) The red dotted line is a linear fit with the slope corresponding to the critical exponent $z = 2.14(2)$, according to the scaling relation $\Gamma \propto \kappa^z$. The green solid line corresponds to 3D-I scaling and the 2D XY model, which both exhibit the exponent $z = 2.0$ [3,100,101]. Note that only the 3D-I model is also consistent with the static critical properties of $Ca_3Ru_2O_7$. The gray data points were not included in the fits.

slope of a linear fit (red dotted line), we derive $z = 2.14(2)$ as the critical exponent, which is close to $z = 2.0$ proposed for the 3D-I model [3,101] and consistent with the $\Gamma(T)$ scaling above. Notably, $z = 2.0$ also corresponds to the 2D XY model [100]. However, since the 3D-I scaling is also compatible with the temperature dependence of the Q width and critical amplitudes at $T > T_N$ of $Ca_3Ru_2O_7$, we consider this model as most appropriate.

IV. DISCUSSION AND CONCLUSION

For Ca_2RuO_4, we revealed that the description of the static critical properties by PL scaling gave only partially satisfactory results, whereas application of the 2D XY model provided a conclusive picture. In more detail, the obtained critical exponent $\beta = 0.158(6)$ is consistent with a 2D XY model with fourfold crystal anisotropy (XYh_4) [71]. The inverse correlation length κ, in principle, could be fitted with different PLs and the 2D XY model. Specifically, the observed saturation of κ in the range between T_N and $T_N + 4$ K was captured by a PL with Q_L dependence, likely indicating the presence of 3D fluctuations close to T_N. Nevertheless, the employed PL fits, with and without κ offset, were not consistent with the 2D nature of Ca_2RuO_4 far above T_N and results from fits of the amplitudes of the critical scattering. Instead, the 2D XY model captured both κ and the amplitude adequately. The resulting Kosterlitz-Thouless temperature $T_{KT} = 87(2)$ K was consistent with the ratio $J'/J = 0.002$ derived from the offset in $\kappa(T)$. Our attempt to describe the amplitude of the critical scattering by PL scaling showed that the functional form does not capture the data appropriately and the extracted critical exponent $\gamma = 0.47(2)$ is not compatible with universal values. Yet, 2D XY scaling captured the critical amplitudes in a broad T range around T_N, in agreement with the Hamiltonian extracted from the magnon dispersion in the ordered phase [50]. The energy width $\Gamma(T)$ is best captured by a PL fit with $z\nu = 1.1(1)$, which is compatible with 3D AFM Heisenberg scaling ($z\nu_{3DH} = 1.067$ [3,94]). However, such a model for

the dynamical critical scaling would be in stark contrast to the static critical behaviors, the magnon dispersion [50], and the quasi-2D character of Ca_2RuO_4. Consequently, we fitted the data with the 2D XY model and $z_{XY} = 2.0$ [100], which also captures the data reasonably well.

In general, a crossover in the critical behavior from 2D XY to Ising scaling close to T_N can be expected in Ca_2RuO_4 due to the orthorhombic terms in the spin Hamiltonian [50]. The observed saturation of $\kappa(T)$ close to T_N might be indicative for a dimensionality crossover to 3D scaling, whereas signatures of such a crossover were less clear in the analysis of the other critical exponents. This apparent absence can be due to the limited instrumental resolution of our TAS measurements and calls for a complementary high-resolution NSE study, focusing on the temperature range in the close vicinity of T_N. Notably, the enhanced energy resolution of NSE previously helped to resolve controversies about the scaling behavior of heavy fermion superconductors [102] and revealed a crossover from Heisenberg to Ising scaling close to T_N in the classical 3D AFM MnF_2 due to uniaxial anisotropy [78]. Moreover, subtle signatures of additional phases, which were proposed to exist in Ca_2RuO_4 above the AFM order, such as orbital order [103,104] and a Jahn-Teller driven spin-nematic phase [105], might be detectable in the critical scaling behavior measured with high-resolution NSE. Apart from that, it will be interesting to probe the existence of possible vortex/antivortex pairs with cryogenic microscopy techniques, such as Lorentz transmission electron microscopy [106], which might be particularly pronounced in thin films of Ca_2RuO_4 [107].

Overall, the distribution in T_N in our sample introduces some uncertainty in our analysis of the critical scattering in Ca_2RuO_4. Nonetheless, we find that our determination of the critical exponents of the Q width, critical amplitudes, and energy width is relatively insensitive to the details of the variance of T_N. Along these lines, we performed fits (not shown here) assuming a difference of ± 0.5 K to our above value of $\Delta T_N = 4.84(1)$ K. The resulting values for ν and z are closely similar to the above ones (difference smaller than the error bars). This is plausible since we fit the data only for $T > T_N + 4$ K, where the impact of the T_N distribution is relatively small. For the critical amplitudes, where the impact of the T_N distribution on the critical exponent is expected to be strongest, as we fit in the range 110–140 K, we find a deviation of only 4% . Also in the case of the critical amplitudes, the change of the critical exponent is smaller than the error bars. This result suggests that even a putative uncertainty in our value of ΔT_N would not critically affect our determination of the critical exponents, corroborating the robustness of our analysis. A definitive determination of the critical behavior close to T_N will require the synthesis of large, monolithic Ca_2RuO_4 single crystals, which appears to be out of reach of the methodologies currently at hand.

For the bilayer compound $Ca_3Ru_2O_7$, which exhibits strong intrabilayer couplings, the critical scaling was only partly compatible with the 2D XY model. Although $\beta = 0.230(6)$ extracted from the temperature dependence of the magnetic (0 0 1) peak matches the expected value for realistic 2D XY systems [69,70], the result should be taken with caution, due to a relatively low point density around $T_{N,1}$ and a possible overlap with the signal from the transition at $T_{N,2}$. While the extracted β is seemingly far from the corresponding value of the 3D-I model ($\beta_{3DI} = 0.327$ [6]), previous works in the context of $Sr_3Ir_2O_7$ pointed out that a significant underestimation of β can arise when the power-law analysis is not narrowly focused around T_N [36], which provides a possible reconciliation between our small β and the proposed 3D-I scaling. The critical scaling of the Q width, amplitude, and energy width above $T_{N,1}$ showed deviations from the 2D XY theory (especially at low temperatures), whereas the 3D-I model captured the data comprehensively. The Ising character of the magnetic correlations likely results from the orthorhombic anisotropy, which eventually drives the magnetic transition at $T_{N,1}$. We remark, however, that in the Γ vs κ plot, 3D-I scaling and the 2D XY model were indistinguishable, due to identical dynamical critical exponents of the universality classes ($z = 2$). Consequently, the 3D-I model provides the most conclusive description of the critical behaviors in $Ca_3Ru_2O_7$, although a partial 2D XY character cannot be excluded. This ambiguity likely reflects the geometry of the exchange bonds in the bilayer structure of $Ca_3Ru_2O_7$, which is intermediate between 2D and 3D cases. The theoretical description of the resulting crossover phenomena and detailed comparison with the experimental data are important challenges for future research.

In conclusion, our study of the critical magnetic correlations has confirmed Ca_2RuO_4 as a realization of the 2D XY AFM on a square lattice. Along with Sr_2IrO_4, which hosts a nearly ideal 2D Heisenberg AFM [34,35], this demonstration illustrates the power of $4d$- and $5d$-electron materials with strongly spin-orbit-entangled magnetic moments as a platform for fundamental research on quantum magnetism.

ACKNOWLEDGMENTS

Financial support by the European Research Council (Com4Com Advanced Grant No. 669550) and from the Deutsche Forschungsgemeinschaft (TRR80 Project No. 107745057) is gratefully acknowledged. Experiments were conducted at TRISP at FRM II in Garching, at FLEXX at BER II in Berlin, and at ThALES at ILL in Grenoble. We acknowledge helpful discussions with J. Bertinshaw, J. Porras, H.-A. Krug von Nidda, and P. Steffens.

APPENDIX A: ENERGY INTEGRATION FOR $Ca_3Ru_2O_7$

Due to the 3D character of the AFM order in $Ca_3Ru_2O_7$ [55], the ideal energy-integration configuration with $k_f \parallel c$ in general cannot be obtained, as Q_L cannot be chosen arbitrarily. To estimate the effects of inelasticity on the experimental Q width we perform a numerical simulation, assuming an intrinsic κ_{in}, and calculate κ_{out}, which nominally corresponds to the width in the experimental Q_H scans. For the simulation we assume a Lorentzian $S(q) = 1/\{1 + [q/\kappa_{in}(T)]^2\}$ with a T-dependent Q width $\kappa_{in}(T) = \kappa_0 t^\nu$, with $\nu = 0.5$ and $\kappa_0 = 0.2$ Å^{-1}. Note that this choice of parameters is close to experimental values extracted from PL fitting in the main text. Further, we assume a Lorentzian $S(\omega) = \Gamma_q/[\Gamma_q^2 + \omega^2]$ with a q-dependent energy width $\Gamma_q = \Gamma(T)\{1 + [q/\kappa_{in}(T)]^2\}$ [27,108,109]. Here, the T-dependent

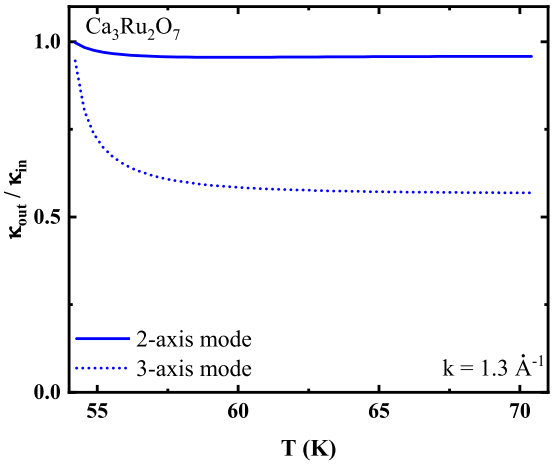

FIG. 13. Simulated ratio of $\kappa_{\rm out}/\kappa_{\rm in}$ vs T in the two- and three-axis mode, respectively (see details in text).

energy width is $\Gamma(T) = \Gamma_0 t^{z\nu}$, with $\Gamma_0 = 1$ meV and $z\nu = 1$. We then calculate the integral [Eq. (5)] in the limits between $-k_{\rm B}T$ and E_i for each q_i in the $Q_{\rm H}$ scan and fit the resulting intensity with a Lorentzian with HWHM $\kappa_{\rm out}$. The results of this simulation are shown in Fig. 13. Notably, for the two-axis mode, the reduction of the measured $\kappa_{\rm out}$ compared to the intrinsic $\kappa_{\rm in}$ is only of the order of a few percent. Such a change in the scaling behavior lies within our statistical error of the critical exponent ν. Hence, we did not correct the two-axis data of $Ca_3Ru_2O_7$ for the integration effect.

For comparison, we conducted the same simulation also for the triple-axis case (Fig. 13), where we added a Gaussian distribution with the energy resolution (± 0.04 meV for $k_i = 1.3$ Å^{-1}) as FWHM. As expected, for the latter case the difference between $\kappa_{\rm in}$ and $\kappa_{\rm out}$ is substantially larger.

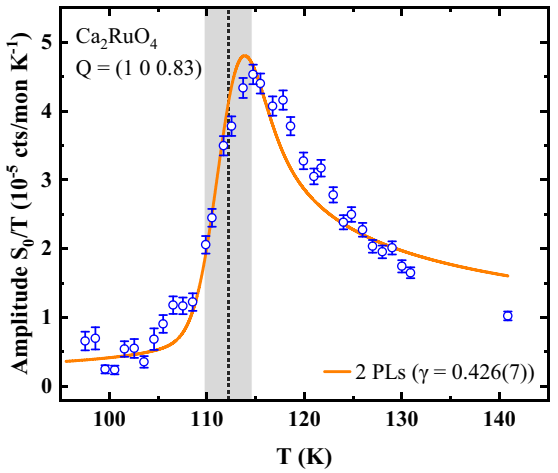

FIG. 14. Peak amplitude $S_0(T)/T$ of Ca_2RuO_4. The orange line corresponds to a PL fit, with $A_-|t|^\gamma$ and $A_+|t|^\gamma$ for $T < T_{\rm N}$ and $T > T_{\rm N}$, respectively. A_- and A_+ are the universal amplitudes. The $T_{\rm N}$ distribution was also taken into account. The extracted critical exponent $\gamma = 0.426(7)$ is close to the value obtained in the main text, where only $A_+|t|^\gamma$ was considered. The black vertical line indicates $T_{\rm N}$ and the gray bar indicates the variance of $T_{\rm N}$.

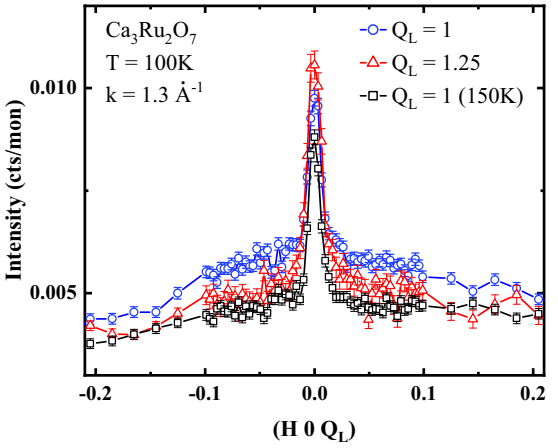

FIG. 15. (H 0 $Q_{\rm L}$) scans in the two-axis mode at $Q_{\rm L} = 1$ and 1.25 for $T = 100$ and 150 K. The corresponding TAS angles are A4 (A3) = 13.8 °(83.1 °) and 17.3 °(81.3 °).

APPENDIX B: CRITICAL SCATTERING AMPLITUDE OF Ca_2RuO_4 BELOW $T_{\rm N}$

Scaling theory predicts for the magnetic susceptibility PL behavior on both sides of $T_{\rm N}$ for an ideal second-order phase transition. Specifically, $\chi = A_-|t|^{-\gamma'}$ for $T < T_{\rm N}$ and $\chi = A_+|t|^{-\gamma}$ with $\gamma = \gamma'$. The resulting critical exponent $\gamma = 0.426(7)$ (Fig. 14) is slightly reduced compared to the exponent extracted from $A_+|t|^\gamma$ in the range 110–140 K [$\gamma = 0.47(2)$], and still far from any universality class. This further supports the notion that the PL fit is not a proper choice for the description of the critical behavior in Ca_2RuO_4.

APPENDIX C: SHARP BACKGROUND PEAK OF $Ca_3Ru_2O_7$

Figure 15 shows that a sharp peak at $H = 0$ is present in the scans around (H 0 $Q_{\rm L}$). This sharp peak is independent of T

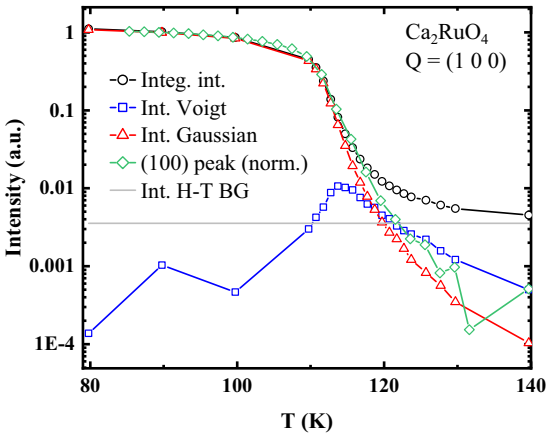

FIG. 16. Integrated intensities of the fit components in the E scans at $Q = (1\,0\,0)$ vs T, including the overall integrated intensity (black), the Voigt profile of the critical scattering (blue), and the resolution-limited Gaussian profile (red). For comparison, we also show the (1 0 0) peak intensity (green), measured with $k_f = 1.5$ Å^{-1} and normalized on the 80-K point of the overall integrated intensity (black). The horizontal gray line indicates the intensity level of the high-temperature (H-T) BG at 170 K.

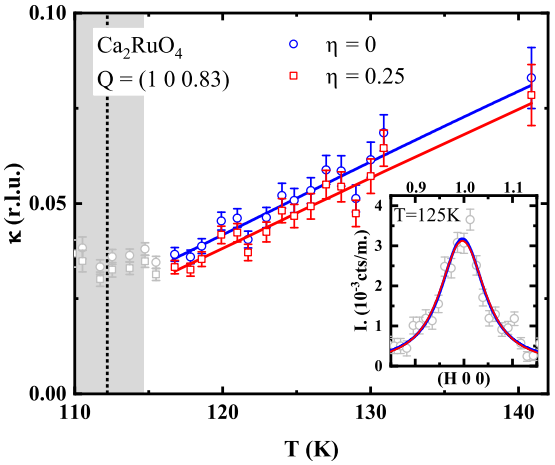

FIG. 17. Comparison of the Q widths κ for a fitting of the Q scans of Ca_2RuO_4 with $\eta = 0$ (blue points) and $\eta = 0.25$ (red points) [Eq. (E1)]. The gray points were not included in the fits. The black vertical line indicates T_N and the gray bar indicates the variance of T_N. The inset shows the corresponding fits at $T = 125$ K.

and Q_L, and thus we assign it to 2D diffuse nuclear scattering from disorder along the c-axis direction in $Ca_3Ru_2O_7$.

APPENDIX D: ENERGY-SCAN INTENSITIES OF Ca_2RuO_4

Figure 16 displays the integrated intensities of the fit components deduced from the energy scans of Ca_2RuO_4 at FLEXX. Upon heating, the intense sharp resolution-limited peak decreases significantly while above ≈116 K the broad critical component is gradually taking over almost all the spectral weight besides the elastic component. For comparison we added the (1 0 0) peak intensity measured with $k = 1.5$ Å^{-1} and normalized on the 80-K point of the entire integrated intensity. The scaling of the normalized (1 0 0) peak resembles that of the sharp component, and thus we assign the latter to elastic magnetic scattering from the (1 0 0) still present above T_N due to the broad transition.

APPENDIX E: PEAK SHAPE OF Q SCANS

As described in the Methods section, for the analysis of the Q scans, we fitted the data with a Voigt profile, i.e., a convolution of a Gaussian (instrumental resolution) and a simple Lorentzian function [Eq. (3)]. Beyond this approximation, which is commonly used to describe critical scattering [20,35,36], subtle deviations from the Lorentzian form were proposed, accounting for the critical exponent η [1,4]:

$$\chi'(\boldsymbol{q}) = \frac{\chi'(\boldsymbol{0})}{[1 + q^2(1-\eta/2)^{-1}/\kappa^2]^{1-\eta/2}}, \tag{E1}$$

with $\eta \approx 0$ and 0.25 predicted for 3D and 2D universality classes [4], respectively. Hence, the peak shape of the Q scans also includes information on the critical behavior of the system. For bilayer $Ca_3Ru_2O_7$, the 3D character of the critical fluctuations above T_N suggests $\eta \approx 0$ consistent with the well-matching Voigt fits (Fig. 6). For single-layer Ca_2RuO_4, one would generally expect deviations from a simple Voigt function due to the 2D character of the fluctuations. However, we find that in our case fits with $\eta = 0$ and 0.25 yield peak shapes that are essentially the same within the experimental error of our data (insets in Fig. 17). Nevertheless, we carried out the analysis of the full set of Q scans not only for $\eta = 0$ [Ornstein-Zernike form, Eq. (E1)], but also for $\eta = 0.25$ (2D XY model [11]). As can be seen in Fig. 17, the effect of η on our Q widths is small, and is negligible with respect to the corresponding scaling behavior of $\kappa(T)$. Specifically, we obtain from 2D XY fits [Eq. (6)] on the non-Lorentzian data ($\eta = 0.25$) for the Kosterlitz-Thouless temperature $T_{KT} = 88(2)$ K for Ca_2RuO_4, which coincides within the statistical errors with the value discussed in the main text. Furthermore, we remark that in general a variety of other factors such as a non-Gaussian instrumental resolution and surface effects [110,111] can also influence the peak shape, which generally make the determination of η challenging.

[1] M. E. Fisher and R. J. Burford, Theory of critical-point scattering and correlations. I. The Ising model, Phys. Rev. **156**, 583 (1967).

[2] H. E. Stanley, *Introduction to Phase Transitions and Critical Phenomena*, International Series of Monographs on Physics (Oxford University, New York, 1971).

[3] P. C. Hohenberg and B. I. Halperin, Theory of dynamic critical phenomena, Rev. Mod. Phys. **49**, 435 (1977).

[4] M. F. Collins, *Magnetic Critical Scattering*, Oxford Series on Neutron Scattering in Condensed Matter (Oxford University, New York, 1989).

[5] B. I. Halperin and P. C. Hohenberg, Scaling laws for dynamic critical phenomena, Phys. Rev. **177**, 952 (1969).

[6] A. Pelissetto and E. Vicari, Critical phenomena and renormalization-group theory, Phys. Rep. **368**, 549 (2002).

[7] R. B. Griffiths, Dependence of Critical Indices on a Parameter, Phys. Rev. Lett. **24**, 1479 (1970).

[8] L. P. Kadanoff, Critical behavior: Universality and scaling, in *From Order to Chaos*, World Scientific Series on Nonlinear Science Series A Vol. 1, edited by L. P. Kadanoff (World Scientific, Singapore, 1993).

[9] V. L. Berezinsky, Destruction of long-range order in one-dimensional and two-dimensional systems possessing a continuous symmetry group. II. Quantum systems, Sov. Phys. JETP **34**, 610 (1972).

[10] J. M. Kosterlitz and D. J. Thouless, Ordering, metastability and phase transitions in two-dimensional systems, J. Phys. C **6**, 1181 (1973).

[11] J. M. Kosterlitz, The critical properties of the two-dimensional XY model, J. Phys. C **7**, 1046 (1974).

[12] D. J. Bishop and J. D. Reppy, Study of the Superfluid Transition in Two-Dimensional ^{4}He Films, Phys. Rev. Lett. **40**, 1727 (1978).

[13] J. M. Kosterlitz, Superfluidity in thin films of ^{4}He, J. Low Temp. Phys. **201**, 541 (2020).

[14] D. J. Resnick, J. C. Garland, J. T. Boyd, S. Shoemaker, and R. S. Newrock, Kosterlitz-Thouless Transition in Proximity-Coupled Superconducting Arrays, Phys. Rev. Lett. **47**, 1542 (1981).

[15] Ch. Leemann, Ph. Lerch, G.-A. Racine, and P. Martinoli, Vortex Dynamics and Phase Transitions in a Two-Dimensional Array of Josephson Junctions, Phys. Rev. Lett. **56**, 1291 (1986).

[16] L. P. Regnault and J. Rossat-Mignod, Phase transitions in quasi two-dimensional planar magnets, in *Magnetic Properties of Layered Transition Metal Compounds*, Physics and Chemistry of Materials with Low-Dimensional Structures, edited by L. J. Jongh (Springer, New York, 1990).

[17] K. Hirakawa, H. Yoshizawa, and K. Ubukoshi, Neutron scattering study of the phase transition in two-dimensional planar ferromagnet K_2CuF_4, J. Phys. Soc. Jpn. **51**, 2151 (1982).

[18] S. T. Bramwell, P. C. W. Holdsworth, and M. T. Hutchings, Static and dynamic magnetic properties of Rb_2CrCl_4: Ideal 2D-XY behaviour in a layered magnet, J. Phys. Soc. Jpn. **64**, 3066 (1995).

[19] H. M. Rønnow, A. R. Wildes, and S. T. Bramwell, Magnetic correlations in the 2D honeycomb antiferromagnet $MnPS_3$, Phys. B: Condens. Matter **276–278**, 676 (2000).

[20] E. S. Klyushina, J. Reuther, L. Weber, A. T. M. N. Islam, J. S. Lord, B. Klemke, M. Månsson, S. Wessel, and B. Lake, Signatures for Berezinskii-Kosterlitz-Thouless critical behavior in the planar antiferromagnet $BaNi_2V_2O_8$, Phys. Rev. B **104**, 064402 (2021).

[21] G. Shirane, J. M. Tranquada, and S. M. Shapiro, *Neutron Scattering with a Triple-Axis Spectrometer: Basic Techniques* (Cambridge University, Cambridge, England, 2002).

[22] T. Chatterji, *Neutron Scattering from Magnetic Materials*, 1st ed. (Elsevier, Amsterdam, 2006).

[23] G. L. Squires, *Introduction to the Theory of Thermal Neutron Scattering*, Dover Books on Physics (Dover, New York, 1996).

[24] J. Als-Nielsen, Neutron scattering and spatial correlation near the critical point, in *Phase Transitions and Critical Phenomena*, edited by C. Domb and M. S. Green (Academic, London, 1976).

[25] O. W. Dietrich, J. Als-Nielsen, and L. Passell, Neutron scattering from the Heisenberg ferromagnets EuO and EuS. III. Spin dynamics of EuO, Phys. Rev. B **14**, 4923 (1976).

[26] P. Böni and G. Shirane, Paramagnetic neutron scattering from the Heisenberg ferromagnet EuO, Phys. Rev. B **33**, 3012 (1986).

[27] A. Tucciarone, H. Y. Lau, L. M. Corliss, A. Delapalme, and J. M. Hastings, Quantitative analysis of inelastic scattering in two-crystal and three-crystal neutron spectrometry; Critical scattering from $RbMnF_3$, Phys. Rev. B **4**, 3206 (1971).

[28] R. Coldea, R. A. Cowley, T. G. Perring, D. F. McMorrow, and B. Roessli, Critical behavior of the three-dimensional Heisenberg antiferromagnet $RbMnF_3$, Phys. Rev. B **57**, 5281 (1998).

[29] R. J. Christianson, R. L. Leheny, R. J. Birgeneau, and R. W. Erwin, Critical dynamics of a spin-5/2 two-dimensional isotropic antiferromagnet, Phys. Rev. B **63**, 140401(R) (2001).

[30] Y. J. Kim, R. J. Birgeneau, F. C. Chou, R. W. Erwin, and M. A. Kastner, Critical Spin Dynamics of the 2D Quantum Heisenberg Antiferromagnets $Sr_2CuO_2Cl_2$ and $Sr_2Cu_3O_4Cl_2$, Phys. Rev. Lett. **86**, 3144 (2001).

[31] B. Keimer, N. Belk, R. J. Birgeneau, A. Cassanho, C. Y. Chen, M. Greven, M. A. Kastner, A. Aharony, Y. Endoh, R. W. Erwin, and G. Shirane, Magnetic excitations in pure, lightly doped, and weakly metallic La_2CuO_4, Phys. Rev. B **46**, 14034 (1992).

[32] B. J. Kim, H. Jin, S. J. Moon, J.-Y. Kim, B.-G. Park, C. S. Leem, J. Yu, T. W. Noh, C. Kim, S.-J. Oh, J.-H. Park, V. Durairaj, G. Cao, and E. Rotenberg, Novel $J_{\rm eff} = 1/2$ Mott State Induced by Relativistic Spin-Orbit Coupling in Sr_2IrO_4, Phys. Rev. Lett. **101**, 076402 (2008).

[33] B. J. Kim, H. Ohsumi, T. Komesu, S. Sakai, T. Morita, H. Takagi, and T. Arima, Phase-sensitive observation of a spin-orbital Mott state in Sr_2IrO_4, Science **323**, 1329 (2009).

[34] S. Fujiyama, H. Ohsumi, T. Komesu, J. Matsuno, B. J. Kim, M. Takata, T. Arima, and H. Takagi, Two-Dimensional Heisenberg Behavior of $J_{\rm eff} = 1/2$ Isospins in the Paramagnetic State of the Spin-Orbital Mott Insulator Sr_2IrO_4, Phys. Rev. Lett. **108**, 247212 (2012).

[35] J. G. Vale, S. Boseggia, H. C. Walker, R. Springell, Z. Feng, E. C. Hunter, R. S. Perry, D. Prabhakaran, A. T. Boothroyd, S. P. Collins, H. M. Rønnow, and D. F. McMorrow, Importance of XY anisotropy in Sr_2IrO_4 revealed by magnetic critical scattering experiments, Phys. Rev. B **92**, 020406(R) (2015).

[36] J. G. Vale, S. Boseggia, H. C. Walker, R. S. Springell, E. C. Hunter, R. S. Perry, S. P. Collins, and D. F. McMorrow, Critical fluctuations in the spin-orbit Mott insulator $Sr_3Ir_2O_7$, J. Phys.: Condens. Matter **31**, 185803 (2019).

[37] G. Cao and L. de Long, *Frontiers of 4d- and 5d-Transition Metal Oxides* (World Scientific, Singapore, 2013).

[38] I. Markovic, M. D. Watson, O. J. Clark, F. Mazzola, E. Abarca Morales, C. A. Hooley, H. Rosner, C. M. Polley, T. Balasubramanian, S. Mukherjee, N. Kikugawa, D. A. Sokolov, A. P. Mackenzie, and P. D. C. King, Electronically driven spin-reorientation transition of the correlated polar metal $Ca_3Ru_2O_7$, Proc. Natl. Acad. Sci. USA **117**, 15524 (2020).

[39] S. A. Grigera, R. S. Perry, A. J. Schofield, M. Chiao, S. R. Julian, G. G. Lonzarich, S. I. Ikeda, Y. Maeno, A. J. Millis, and A. P. Mackenzie, Magnetic field-tuned quantum criticality in the metallic ruthenate $Sr_3Ru_2O_7$, Science **294**, 329 (2001).

[40] M. Horio, Q. Wang, V. Granata, K. P. Kramer, Y. Sassa, S. Jöhr, D. Sutter, A. Bold, L. Das, Y. Xu, R. Frison, R. Fittipaldi, T. K. Kim, C. Cacho, J. E. Rault, P. Le Fèvre, F. Bertran, N. C. Plumb, M. Shi, A. Vecchione *et al.*, Electronic reconstruction forming a C2-symmetric Dirac semimetal in $Ca_3Ru_2O_7$, npj Quantum Mater. **6**, 29 (2021).

[41] Y. Sidis, M. Braden, P. Bourges, B. Hennion, S. NishiZaki, Y. Maeno, and Y. Mori, Evidence for Incommensurate Spin Fluctuations in Sr_2RuO_4, Phys. Rev. Lett. **83**, 3320 (1999).

[42] Y. Maeno, H. Hashimoto, K. Yoshida, S. Nishizaki, T. Fujita, J. G. Bednorz, and F. Lichtenberg, Superconductivity in a layered perovskite without copper, Nature (London) **372**, 532 (1994).

[43] G. Khaliullin, Excitonic Magnetism in Van Vleck-Type d^4 Mott Insulators, Phys. Rev. Lett. **111**, 197201 (2013).

[44] A. Akbari and G. Khaliullin, Magnetic excitations in a spin-orbit-coupled d^4 Mott insulator on the square lattice, Phys. Rev. B **90**, 035137 (2014).

[45] M. Braden, G. André, S. Nakatsuji, and Y. Maeno, Crystal and magnetic structure of Ca_2RuO_4: Magnetoelastic coupling and the metal-insulator transition, Phys. Rev. B **58**, 847 (1998).

[46] C. S. Alexander, G. Cao, V. Dobrosavljevic, S. McCall, J. E. Crow, E. Lochner, and R. P. Guertin, Destruction of the Mott insulating ground state of Ca_2RuO_4 by a structural transition, Phys. Rev. B **60**, R8422 (1999).

[47] S. Nakatsuji and Y. Maeno, Synthesis and single-crystal growth of $Ca_{2-x}Sr_xRuO_4$, J. Solid State Chem. **156**, 26 (2001).

[48] H. Gretarsson, H. Suzuki, H. Kim, K. Ueda, M. Krautloher, B. J. Kim, H. Yavaş, G. Khaliullin, and B. Keimer, Observation of spin-orbit excitations and Hund's multiplets in Ca_2RuO_4, Phys. Rev. B **100**, 045123 (2019).

[49] S.-M. Souliou, J. Chaloupka, G. Khaliullin, G. Ryu, A. Jain, B. J. Kim, M. Le Tacon, and B. Keimer, Raman Scattering from Higgs Mode Oscillations in the Two-Dimensional Antiferromagnet Ca_2RuO_4, Phys. Rev. Lett. **119**, 067201 (2017).

[50] A. Jain, M. Krautloher, J. Porras, G. H. Ryu, D. P. Chen, D. L. Abernathy, J. T. Park, A. Ivanov, J. Chaloupka, G. Khaliullin, B. Keimer, and B. J. Kim, Higgs mode and its decay in a two-dimensional antiferromagnet, Nat. Phys. **13**, 633 (2017).

[51] S. McCall, G. Cao, and J. E. Crow, Impact of magnetic fields on anisotropy in $Ca_3Ru_2O_7$, Phys. Rev. B **67**, 094427 (2003).

[52] Y. Yoshida, S.-I. Ikeda, H. Matsuhata, N. Shirakawa, C. H. Lee, and S. Katano, Crystal and magnetic structure of $Ca_3Ru_2O_7$, Phys. Rev. B **72**, 054412 (2005).

[53] B. Bohnenbuck, I. Zegkinoglou, J. Strempfer, C. Schüßler-Langeheine, C. S. Nelson, P. Leininger, H.-H. Wu, E. Schierle, J. C. Lang, G. Srajer, S. I. Ikeda, Y. Yoshida, K. Iwata, S. Katano, N. Kikugawa, and B. Keimer, Magnetic structure and orbital state of $Ca_3Ru_2O_7$ investigated by resonant x-ray diffraction, Phys. Rev. B **77**, 224412 (2008).

[54] X. Ke, T. Hong, J. Peng, S. E. Nagler, G. E. Granroth, M. D. Lumsden, and Z. Q. Mao, Spin-wave excitation in the antiferromagnetic bilayer ruthenate $Ca_3Ru_2O_7$, Phys. Rev. B **84**, 014422 (2011).

[55] J. Bertinshaw, M. Krautloher, H. Suzuki, H. Takahashi, A. Ivanov, H. Yavaş, B. J. Kim, H. Gretarsson, and B. Keimer, Spin and charge excitations in the correlated multiband metal $Ca_3Ru_2O_7$, Phys. Rev. B **103**, 085108 (2021).

[56] T. Keller, K. Habicht, H. Klann, M. Ohl, H. Schneider, and B. Keimer, The NRSE-TAS spectrometer at the FRM-2, Appl. Phys. A **74**, s332 (2002).

[57] T. Keller and B. Keimer, TRISP: Three axes spin echo spectrometer, JLSRF **1**, A37 (2015).

[58] M. D. Le, D. L. Quintero-Castro, R. Toft-Petersen, F. Groitl, M. Skoulatos, K. C. Rule, and K. Habicht, Gains from the upgrade of the cold neutron triple-axis spectrometer FLEXX at the BER-II reactor, Nucl. Instrum. Methods Phys. Res., Sect. A **729**, 220 (2013).

[59] H. Trepka, M. Boehm, M. Hepting, M. J. Krautloher, and J. Porras, Complex magnetic fluctuations in Ca_2RuO_4 above the Néel temperature. Institut Laue-Langevin (ILL), ILL experimental report (2020), doi:10.5291/ILL-DATA.4-03-1738.

[60] M. Boehm, S. Roux, A. Hiess, and J. Kulda, ThALES—towards the next generation cold neutron three-axis spectrometer, J. Magn. Magn. Mater. **310**, e965 (2007).

[61] A. Boothroyd, *Principles of Neutron Scattering from Condensed Matter* (Oxford University, New York, 2020).

[62] R. J. Birgeneau, J. Skalyo, and G. Shirane, Critical Magnetic Scattering in K_2NiF_4, Phys. Rev. B **3**, 1736 (1971).

[63] D. G. Porter, V. Granata, F. Forte, S. Di Matteo, M. Cuoco, R. Fittipaldi, A. Vecchione, and A. Bombardi, Magnetic anisotropy and orbital ordering in Ca_2RuO_4, Phys. Rev. B **98**, 125142 (2018).

[64] S. Nakatsuji, S.-I. Ikeda, and Y. Maeno, Ca_2RuO_4: New Mott insulators of layered ruthenate, J. Phys. Soc. Jpn. **66**, 1868 (1997).

[65] S. Kunkemöller, D. Khomskii, P. Steffens, A. Piovano, A. A. Nugroho, and M. Braden, Highly Anisotropic Magnon Dispersion in Ca_2RuO_4: Evidence for Strong Spin Orbit Coupling, Phys. Rev. Lett. **115**, 247201 (2015).

[66] O. W. Dietrich, Critical magnetic fluctuations in MnF_2, J. Phys. C **2**, 2022 (1969).

[67] A. Lupascu, J. P. Clancy, H. Gretarsson, Z. Nie, J. Nichols, J. Terzic, G. Cao, S. S. A. Seo, Z. Islam, M. H. Upton, J. Kim, D. Casa, T. Gog, A. H. Said, V. M. Katukuri, H. Stoll, L. Hozoi, J. van den Brink, and Y.-J. Kim, Tuning Magnetic Coupling in Sr_2IrO_4 Thin Films with Epitaxial Strain, Phys. Rev. Lett. **112**, 147201 (2014).

[68] J. Porras, J. Bertinshaw, H. Liu, G. Khaliullin, N. H. Sung, J.-W. Kim, S. Francoual, P. Steffens, G. Deng, M. M. Sala, A. Efimenko, A. Said, D. Casa, X. Huang, T. Gog, J. Kim, B. Keimer, and B. J. Kim, Pseudospin-lattice coupling in the spin-orbit Mott insulator Sr_2IrO_4, Phys. Rev. B **99**, 085125 (2019).

[69] S. T. Bramwell and P. C. W. Holdsworth, Magnetization and universal sub-critical behaviour in two-dimensional XY magnets, J. Phys.: Condens. Matter **5**, L53 (1993).

[70] S. T. Bramwell and P. C. W. Holdsworth, Universality in two–dimensional magnetic systems, J. Appl. Phys. **73**, 6096 (1993).

[71] A. Taroni, S. T. Bramwell, and P. C. W. Holdsworth, Universal window for two-dimensional critical exponents, J. Phys.: Condens. Matter **20**, 275233 (2008).

[72] A. Zheludev, software:ResLib 3.4 (2009), Brookhaven National Laboratory, Oak Ridge National Laboratory and ETH Zuerich, https://neutron.ethz.ch/Methods/reslib.html.

[73] T. Weber, R. Georgii, and P. Böni, Takin: An open-source software for experiment planning, visualisation, and data analysis, SoftwareX **5**, 121 (2016).

[74] F. Mezei, *Neutron Spin Echo: Proceedings of a Laue-Langevin Institut Workshop Grenoble, October 15-16, 1979*, Lecture Notes in Physics Vol. 128 (Springer-Verlag, Berlin, 1980).

[75] T. J. Keller, H. Trepka, K. Habicht, and B. Keimer, Neutron spin-echo instrumentation for magnetic scattering, Phys. Status Solidi B, **259**, 2100164 (2021).

[76] F. Mezei, Role of Spin-Nonconserving Forces in the Critical Dynamics of Fe at the Curie Point, Phys. Rev. Lett. **49**, 1096 (1982).

[77] F. Mezei, Critical dynamics in isotropic ferromagnets, J. Magn. Magn. Mater. **45**, 67 (1984).

[78] K. F. Tseng, T. Keller, A. C. Walters, R. J. Birgeneau, and B. Keimer, Neutron spin-echo study of the critical dynamics of spin-5/2 antiferromagnets in two and three dimensions, Phys. Rev. B **94**, 014424 (2016).

[79] R. J. Birgeneau, R. A. Cowley, G. Shirane, J. A. Tarvin, and H. J. Guggenheim, Spin fluctuations in random magnetic-nonmagnetic two-dimensional antiferromagnets. II. Heisenberg percolation, Phys. Rev. B **21**, 317 (1980).

[80] R. A. Cowley, R. J. Birgeneau, G. Shirane, H. J. Guggenheim, and H. Ikeda, Spin fluctuations in random magnetic-nonmagnetic two-dimensional antiferromagnets. III. An Ising system, Phys. Rev. B **21**, 4038 (1980).

[81] J. Als-Nielsen, S. T. Bramwell, M. T. Hutchings, G. J. McIntyre, and D. Visser, Neutron scattering investigation of the static critical properties of Rb_2CrCl_4, J. Phys.: Condens. Matter **5**, 7871 (1993).

[82] S. Chakravarty, B. I. Halperin, and D. R. Nelson, Low-Temperature Behavior of Two-Dimensional Quantum Antiferromagnets, Phys. Rev. Lett. **60**, 1057 (1988).

[83] S. Chakravarty, B. I. Halperin, and D. R. Nelson, Two-dimensional quantum Heisenberg antiferromagnet at low temperatures, Phys. Rev. B **39**, 2344 (1989).

[84] P. Hasenfratz and F. Niedermayer, The exact correlation length of the antiferromagnetic $d = 2 + 1$ Heisenberg model at low temperatures, Phys. Lett. B **268**, 231 (1991).

[85] F. G. Mertens, A. R. Bishop, G. M. Wysin, and C. Kawabata, Dynamical correlations from mobile vortices in two-dimensional easy-plane ferromagnets, Phys. Rev. B **39**, 591 (1989).

[86] T. Roscilde, A. Cuccoli, and P. Verrucchi, Phase transitions in anisotropic two-dimensional quantum antiferromagnets, Phys. Status Solidi B **236**, 433 (2003).

[87] A. Cuccoli, T. Roscilde, R. Vaia, and P. Verrucchi, Detection of XY Behavior in Weakly Anisotropic Quantum Antiferromagnets on the Square Lattice, Phys. Rev. Lett. **90**, 167205 (2003).

[88] A. Cuccoli, T. Roscilde, V. Tognetti, R. Vaia, and P. Verrucchi, Quantum Monte Carlo study of S=1/2 weakly anisotropic antiferromagnets on the square lattice, Phys. Rev. B **67**, 104414 (2003).

[89] M. Heinrich, H.-A. Krug von Nidda, A. Loidl, N. Rogado, and R. J. Cava, Potential Signature of a Kosterlitz-Thouless Transition in $BaNi_2V_2O_8$, Phys. Rev. Lett. **91**, 137601 (2003).

[90] X. Ke, J. Peng, D. J. Singh, T. Hong, W. Tian, C. R. Dela Cruz, and Z. Q. Mao, Emergent electronic and magnetic state in $Ca_3Ru_2O_7$ induced by Ti doping, Phys. Rev. B **84**, 201102(R) (2011).

[91] G. Cao, S. McCall, J. E. Crow, and R. P. Guertin, Observation of a Metallic Antiferromagnetic Phase and Metal to Nonmetal Transition in $Ca_3Ru_2O_7$, Phys. Rev. Lett. **78**, 1751 (1997).

[92] P. Gaveau, J. P. Boucher, L. P. Regnault, and Y. Henry, Magnetic–field dependence of the phosphorus nuclear spin–relaxation rate in the quasi–two–dimensional XY antiferromagnet $BaNi_2(PO_4)_2$, J. Appl. Phys. **69**, 6228 (1991).

[93] M. Hemmida, H.-A. Krug von Nidda, N. Büttgen, A. Loidl, L. K. Alexander, R. Nath, A. V. Mahajan, R. F. Berger, R. J. Cava, Y. Singh, and D. C. Johnston, Vortex dynamics and frustration in two-dimensional triangular chromium lattices, Phys. Rev. B **80**, 054406 (2009).

[94] M. Campostrini, M. Hasenbusch, A. Pelissetto, P. Rossi, and E. Vicari, Critical exponents and equation of state of the three-dimensional Heisenberg universality class, Phys. Rev. B **65**, 144520 (2002).

[95] G. F. Mazenko and O. T. Valls, Dynamic critical exponent z in some two-dimensional models, Phys. Rev. B **24**, 1419 (1981).

[96] D. L. Huber, Dynamics of spin vortices in two-dimensional planar magnets, Phys. Rev. B **26**, 3758 (1982).

[97] F. G. Mertens, A. R. Bishop, G. M. Wysin, and C. Kawabata, Vortex Signatures in Dynamic Structure Factors for Two-Dimensional Easy-Plane Ferromagnets, Phys. Rev. Lett. **59**, 117 (1987).

[98] M. T. Hutchings, P. Day, E. Janke, and R. Pynn, Critical spin dynamics in Rb_2CrCl_4: A nearly two-dimensional easy-plane ferromagnet, J. Magn. Magn. Mater. **54–57**, 673 (1986).

[99] L. P. Regnault, J. P. Boucher, J. Rossat-Mignod, J. Bouillot, R. Pynn, J. Y. Henry, and J. P. Renard, Nonlinear excitations in 1*d* and 2*d* magnetic systems, Physica B+C **136**, 329 (1986).

[100] L. M. Jensen, B. J. Kim, and P. Minnhagen, Dynamic critical exponent of two-, three-, and four-dimensional XY models with relaxational and resistively shunted junction dynamics, Phys. Rev. B **61**, 15412 (2000).

[101] M. Hasenbusch, Dynamic critical exponent z of the three-dimensional Ising universality class: Monte Carlo simulations of the improved Blume-Capel model, Phys. Rev. E **101**, 022126 (2020).

[102] F. Haslbeck, S. Säubert, M. Seifert, C. Franz, M. Schulz, A. Heinemann, T. Keller, P. Das, J. D. Thompson, E. D. Bauer, C. Pfleiderer, and M. Janoschek, Ultrahigh-resolution neutron spectroscopy of low-energy spin dynamics in UGe_2, Phys. Rev. B **99**, 014429 (2019).

[103] I. Zegkinoglou, J. Strempfer, C. S. Nelson, J. P. Hill, J. Chakhalian, C. Bernhard, J. C. Lang, G. Srajer, H. Fukazawa, S. Nakatsuji, Y. Maeno, and B. Keimer, Orbital Ordering Transition in Ca_2RuO_4 Observed with Resonant X-Ray Diffraction, Phys. Rev. Lett. **95**, 136401 (2005).

[104] J. Lotze and M. Daghofer, Suppression of effective spin-orbit coupling by thermal fluctuations in spin-orbit coupled antiferromagnets, Phys. Rev. B **104**, 045125 (2021).

[105] H. Liu and G. Khaliullin, Pseudo-Jahn-Teller Effect and Magnetoelastic Coupling in Spin-Orbit Mott Insulators, Phys. Rev. Lett. **122**, 057203 (2019).

[106] Y. Togawa, T. Akashi, H. Kasai, G. W. Paterson, S. McVitie, Y. Kousaka, H. Shinada, J.-I. Kishine, and J. Akimitsu, Formations of narrow stripes and vortex-antivortex pairs in a quasi-two-dimensional ferromagnet K_2CuF_4, J. Phys. Soc. Jpn. **90**, 014702 (2021).

[107] C. Dietl, S. K. Sinha, G. Christiani, Y. Khaydukov, T. Keller, D. Putzky, S. Ibrahimkutty, P. Wochner, G. Logvenov, P. A. van Aken, B. J. Kim, and B. Keimer, Tailoring the electronic properties of Ca_2RuO_4 via epitaxial strain, Appl. Phys. Lett. **112**, 031902 (2018).

[108] M. P. Schulhof, P. Heller, R. Nathans, and A. Linz, Critical magnetic scattering in manganese fluoride, Phys. Rev. B **1**, 2304 (1970).

[109] P. Steffens, O. Friedt, Y. Sidis, P. Link, J. Kulda, K. Schmalzl, S. Nakatsuji, and M. Braden, Magnetic excitations in the metallic single-layer ruthenates $Ca_{2-x}Sr_xRuO_4$ studied by inelastic neutron scattering, Phys. Rev. B **83**, 054429 (2011).

[110] M. Papoular, M. D. Núñez-Regueiro, and M. Altarelli, Two-length-scale problem in critical scattering: Narrow-component line shape, Phys. Rev. B **56**, 166 (1997).

[111] R. A. Cowley and S. M. Shapiro, Structural phase transitions, J. Phys. Soc. Jpn. **75**, 111001 (2006).